CHARACTERIZATION OF UTA HYPERSONIC

SHOCK TUNNEL

by

DEREK GLENN LEAMON

Presented to the Faculty of the Graduate School of

The University of Texas at Arlington in Partial Fulfillment

of the Requirements

for the Degree of

MASTER OF SCIENCE IN AEROSPACE ENGINEERING

THE UNIVERSITY OF TEXAS AT ARLINGTON

May 2012

ACKNOWLEDGEMENTS

First and foremost, I would like to thank my family for enabling my pursuit of a Masters degree. Without their emotional and financial support, I would not be in a position that affords me the opportunity to expand my knowledge though higher learning at UTA.

I would like to thank Dr. Don Wilson, who helped me confirm my desire to pursue a Masters degree and gave me the opportunity to work on a thesis project in the reputed Aerodynamics Research Center. My advisor, Dr. Frank Lu, was also immensely friendly and helpful in my pursuit of finishing this study, readily offering a plethora of references and advice relative to my work.

I would like to thank the various professors and their graduate assistants from around campus that graciously gave assistance to my project through the use of their equipment, all at the mere mention of Dr. Frank Lu's name, which demonstrates great respect among his peers. The major contributors were Dr. Rajeshwar in the Department of Chemistry and Biochemistry for use of his furnace and Dr. Luo in the Department of Mechanical and Aerospace Engineering for help in obtaining film micrographs.

A big thanks goes to Kermit Beird and Sam Williams, who selflessly machined several components of my design at no cost to the department. Without their help via CNC machining, the project could not have been completed.

Finally, a very special thanks goes to the late Rod Duke. Without his countless hours of effort in machining, maintenance, guidance, and recommendations, among other assistances, I could never have never have completed this work.

May 9, 2012

ABSTRACT

CHARACTERIZATION OF UTA HYPERSONIC

SHOCK TUNNEL

Derek Glenn Leamon, M.S.

The University of Texas at Arlington, 2012

Supervising Professor: Frank K. Lu

Characterization of a hypersonic shock tunnel was performed under low enthalpy conditions. A rake was designed and fabricated to measure pitot pressure and heat flux at three axial locations in the test section. Pitot pressures at three locations provided an indication of the inviscid core. Thin film RTD sensors with a fast response time were fabricated to measure the heat flux under these low enthalpy conditions. The Cook-Felderman algorithm was used to estimate the heat flux from the temperature history. Results for the first millisecond of test time showed a probe tip surface temperature increase of 15-20 K and a calculated heat flux in the inviscid core of 9.93 ± 0.56 W/cm^2.

TABLE OF CONTENTS

LIST OF ILLUSTRATIONS

LIST OF TABLES

NOMENCLATURE

A	cross-sectional area
a	speed of sound
c	specific heat
H	enthalpy
k	thermal conductivity
M	Mach number
P	pressure
$\dot{q}$	heat flux
R	resistance
Re	Reynolds Number
R_g	gas constant of air
T	temperature
t	time
u	velocity
V	voltage
x	axial length
y	height
z	width
α_R	temperature resistance coefficient
β	thermal product
Δ	increment
γ	specific heat ratio
μ	dynamic viscosity
ρ	density
σ	standard deviation

Subscript

air	air used as a medium
gly	glycerin used as a medium
i	input / indice
n	number of points in iteration
o	output
pit	Pitot
ref	reference condition
s	surface
t	stagnation condition
0	ambient condition
1	driven section in front of incident shock
4	driver section
5	driven section behind reflected incident shock
∞	freestream condition

Superscript

°	degree
*	sonic condition

CHAPTER 1

INTRODUCTION

A crucial stage in any aircraft assembly or component design is laboratory testing. It is a means to validate analytically and numerically derived behaviors by simulating flight conditions for a brief period of time on a scaled model. Just as it is important to control test conditions to ensure accurate data collection, it is equally important to understand the test equipment and the limitations they impose when trying to replicate said flight conditions. This can be accomplished with preliminary testing designed specifically to learn the flow properties a model will be exposed to for any set of operating parameters.

During this program, characteristics of the Hypersonic Shock Tunnel (HST) test section was determined experimentally using baseline tunnel operating conditions. The core flow was found by measuring the pressure distribution at multiple planes, which revealed the test section boundary layer and provided a useful Mach number map. Stagnation-point heat transfer rates were simultaneous measured near the axial centerline of the test section utilizing thin-film sensors.

1.1 Objective

The focus of this research is to provide a preliminary indication of the flow quality of a shock tunnel. This effort is one part of a larger collective effort to restore the operational capability of the HST, which was previously decommissioned and disassembled to make room for other projects. These calibration studies, some of which were previously recommended by the initial tunnel designer [1], include taking pitot pressure surveys to determine the test section boundary-layer thickness and core flow, as well as determining heat transfer rates near the centerline of the test section. More specifically, this study concentrated on determining these

1

conditions at multiple axial locations in the test section under low enthalpy conditions while using a throat designed for a freestream Mach number of 10.

To facilitate these goals, a rake capable of measuring pitot pressure spans across the test section at different axial locations was developed. To reduce the number of needed tests and simplify the data reduction process, a means of simultaneously measuring heat transfer rate was incorporated into the design. This system, a rake for housing sensors and a sting for mounting the rake in the test section, will be discussed in detail in Chapter 2.

The HST is limited to a total flow time of a few milliseconds or less. The majority of the test is dominated by transient startup and the blowdown from the high-pressure driver gas behind a short quasi steady-state test period. Due to the brevity of the desired testing period, sensors with sufficiently fast response times must be used. For pressure measurements, this fast response can be accomplished through commercially available transducers. Nine PCB 111A21 pressure transducers of approximately 50 mV/psi sensitivity were utilized for this study. While there are a multitude of commercially available thermocouples and other temperature sensors, most do not have response times and sensitivities suitable for measuring low enthalpy cases in short-duration shock facilities. For this reason, a more arduous technique must be employed. Thin film resistance temperature detectors (RTD) are a common method for determining temperature and heat flux in shock tubes and tunnels due to their fast response time and high sensitivity, making them an ideal selection for this study. These sensors have very thin metallic films mounted on substrates of sufficiently low thermal conductivity. They work on the principle that the film's resistance is linearly proportional to the temperature of the film and that the corresponding voltage response when this resistance is changed is proportional to the square root of time. This voltage response can then be processed to determine the temperature history and the heat flux. To accomplish this, the platinum thin film RTD approach previously developed by Kevin Kinnear in a shock tube at the ARC will be adapted for use in the sting and rake system in this study. Details of the principles behind the thin film RTD used in this program can be found in [2].

1.2 General Operation of the HST

The HST is a reflected shock tunnel that began operation in 1989. It consists of standard shock tunnel components, including a shock tube, interchangeable throat, expansion nozzle, test section, and diffuser with dump tank. The shock tube consists of a high-pressure driver section, a low-pressure driven section, and a short double primary diaphragm section that separates the two sections with intermediate pressure. The driven section is connected to the throat, which is separated from the nozzle by a small secondary diaphragm. This provides increased flexibility in controlling the test section conditions after the expansion nozzle by allowing varying initial pressures between the two sections. The flow terminates after exiting the building through a diffuser and entering a large tank. Figure 1.1(a) shows the general sketch of the HST and Fig. 1.1(b) shows how it exists in 2012.
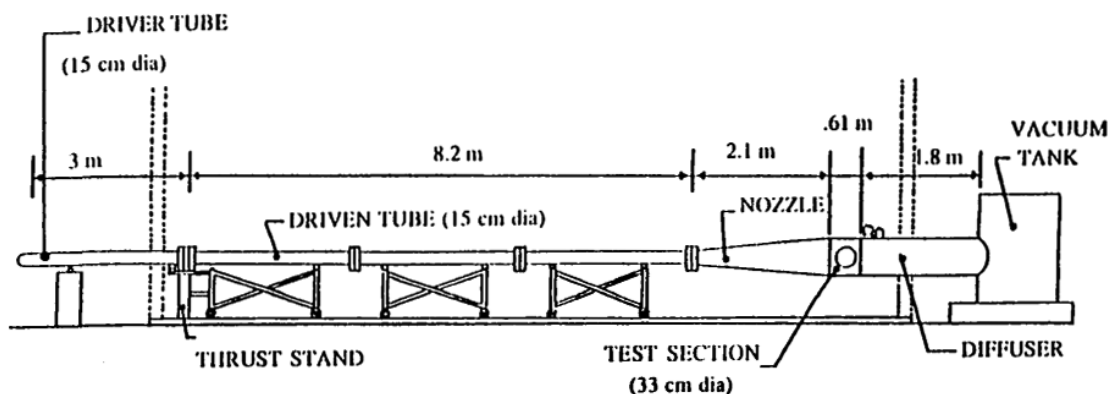
(a)

(b)

Figure 1.1 UTA Hypersonic Shock Tunnel. (a) Schematic [1]. (b) Single-point panoramic view, courtesy of Pravin Vadassery (reverse view).

Typical operation of the HST begins by running a Clark CMB-6 5-stage compressor located in an adjacent building. This compressor supplies up to 14.5 MPa (2100 psi) to a Haskel pump model-55696, which further compresses dry air into a 1 m (3.28 ft) diameter spherical pressure vessel, up to 31 MPa (4500 psi.) This sphere then supplies high pressure air to the driver and double-diaphragm sections of the shock tube. The operating driver pressure, P_4, using air strictly from the sphere is around 20.7 MPa (3000 psi,) which is used exclusively in this study. Depending on the duration of the charging period, pressures as high as 24.1 MPa (3500 psi) can still be achieved, but at the cost of an increasingly large amount of time thanks to diminishing returns from the limited sphere pressure. Pressure in the double diaphragm section is typically kept at half the driver pressure value during charging in order to minimize the possibility of accidental rupture. The primary diaphragms located here can be made from a variety of materials to accommodate a wide range of pressures, but they are typically made of steel for standard operation. Additionally, they are scored with a crossing T pattern, as shown in Figure 1.2, which results in four distinct petals when burst. Ideally, this scoring allows for a controlled burst while minimizing the potential for diaphragm particles to strike models downstream in the test section or for the petals to be ripped off entirely by the reflected shock. This is done by finely adjusting the depth and geometry of the cut.

Figure 1.2 Primary diaphragms before and after successful test.

The driven section is isolated by one of the primary diaphragms and a smaller secondary Mylar diaphragm of 0.254 mm (0.01 in.) thickness, located just in front of the throat. A small Sargent-Welch model-1376 vacuum pump can be used to evacuate this section, typically reaching pressures as low as 0.007 MPa (1.02 psi.) Additionally, this section can then be filled with dry air to a wide range of pressures from a Kellogg American Inc. compressor model DB462-C capable of supplying up to 1.2 MPa (175 psi.) This compressor is also used to control an array of solenoid valves used to read pressures in each section of the HST, as well as valves used in the Haskel pump. For this study, the driven section pressure, P_1, was maintained at the local ambient of 0.102 MPa (14.8 psi) using dry air.

The throat and throat locking mechanism, located directly after the secondary Mylar diaphragm, is made so that the throat can be interchangeable. Since the expansion nozzle exit diameter is fixed, this allows for varying the freestream Mach number by adjusting the throat diameter. The throat used in this study is for $M_\infty=10$ test conditions.

Beyond the expansion nozzle are the test section, diffuser, and dump tank. These sections are connected to a larger Sargent-Welch model-1396 vacuum pump and additional Sargent-Welch model-1376 vacuum pump in order to provide as low a back pressure as possible for the nozzle as it expands the flow. This is imperative to increasing the test duration of the flow. Vacuums achieved in these conjoined sections were limited to 0.0042-0.0044 MPa (0.61-0.64 psi) during this study. For safety, all pumps are isolated from the tunnel by two-port valves before operation.

The testing process is initiated by venting the intermediate pressure from the double-diaphragm section, causing the high pressure to burst through and send a normal shock down the driven section towards the throat. This shock reflects off of the secondary diaphragm and back into the flow, creating stage 5 conditions [3]. These conditions behind the reflected incident shock are also the stagnation conditions for the throat. The high-pressure gas trapped at the upstream end of the throat bursts the diaphragm and initiates the expansion of the flow through the throat and nozzle into the test section. The standard x-t diagram for a reflected

5

shock tunnel is shown in Figure 1.3, with the five standard stages of a reflected shock tube wave propagation indicated in ovals.
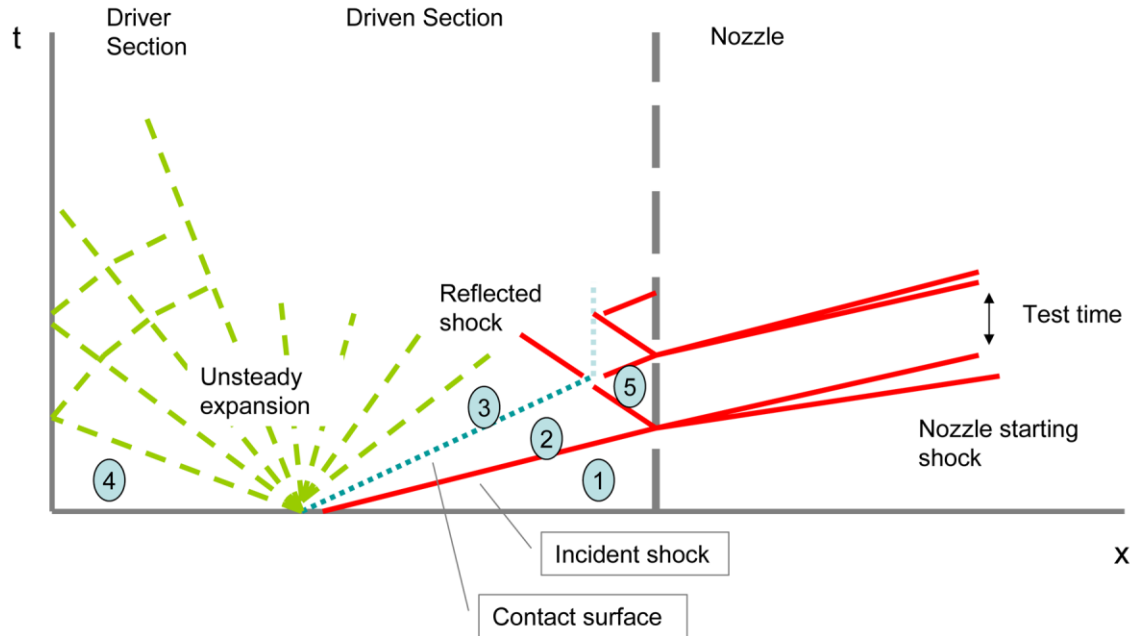
Figure 1.3 Example wave diagram for a reflected shock tunnel [1].

A large number of pressure transducer ports are available to monitor conditions before and during operation. Transducers connected to the driver, double-diaphragm, driven, and test sections of the tunnel allow for safe monitoring and regulation from a remote control room. Ports located along the driven section and expansion nozzle are available for data collection to monitor the flow as it approaches the test section. However, due to the lack of actual transducers available for this study, only two PCB 111A23 transducers were used to measure the normal shock passage at stations 5 and 6 in the driven section [1], which are located 137.16 cm (54 in.) apart. Typically, a sensor used just in front of the secondary diaphragm (station 7) would be used to empirically confirm the pressure behind the reflected shock, P_5, which is also the stagnation pressure for the throat. Due to the unavailability of a transducer for this port, all flow conditions in the shock tube have been calculated from the shock passage.

There are several devices available for data acquisition from sensors at these ports and any sensors associated with the model in the test section. After passing through a PCB model 483A signal conditioner, PCB transducer output can be read by a Tektronix DPO 4054 Digital Phosphor Oscilloscope or by National Instruments TB-2709 data acquisition cards (DAQ) using a National Instruments PXIe-8130 embedded controller. The oscilloscope is capable of 4 channels of data and was used to sample data at 25 MS/s, while the DAQ cards are capable of 8 channels each when processed via National Instruments LabVIEW software. Standard operation during this study used the oscilloscope to measure the two driven section pressure transducers, the RTD response, and to trigger data collection by the DAQ cards for the transducers located in the test section with the single RTD.

1.3 Refurbishment of the HST

Before this study could be performed, the HST required major reassembly and refurbishment of major components that had been damaged or gone missing after its disassembly. This state-of-affairs was due to the rise in interest of pulse detonation research, a waning interest in hypersonic research, and a lack of available laboratory space.

In addition to the standard reassembly and alignment of the double-diaphragm, 3 driven tubes, throat with locker, expansion nozzle, and test section, a number of maintenance and refurbishment procedures had to be performed to restore the HST to working order. The interior of all tunnel components upstream of the diffuser were scrubbed with a radial steel wire wheel brush to remove residue from previous tests and inactivity.

The diffuser section itself, which previously slid in and out of another diffuser pipe section passing through the wall to the dump tank, could not be found during reassembly. It was replaced with a fixed diffuser section containing five 10.16 cm (4 in.) diameter ports for instrumentation mounting purposes, designed by team lead Tiago Rolim.

The interior of the dump tank was treated for corrosion by Enrust, for rust treatment and prevention. Rust was most likely caused by the untreated interior's exposure to years of humidity due to a broken safety valve which allows excess pressure to escape during testing

that could otherwise damage the sensitive sensors in the test section by exposing them to much longer durations of high pressure after the concluded tests. This safety valve, which is held closed by a spring, was repaired as well.

From the safety valve, schedule 40 steel piping connecting the dump tank to the Sargent-Welch model-1396 vacuum pump needed to be replaced due to missing parts and severe damage to some fittings. The pump itself was given maintenance and thoroughly sealed with room temperature vulcanization (RTV) silicone to minimize leaks.

The three transducers for monitoring and regulating pressure in the driver, double-diaphragm, and driven sections were all replaced with Omegadyne Inc. model MMA5.0KVP4K1T3A5 transducers due to failure of the previous transducers during initial testing after restoring tunnel operation.

Lastly, some components of the throat locking mechanism, which secures the throat to the expansion nozzle, were replaced with a single piece to simplify the procedure needed to replace the secondary diaphragm. The part is a stainless steel disk designed again by team lead Tiago Rolim, as shown in Figure 1.4.
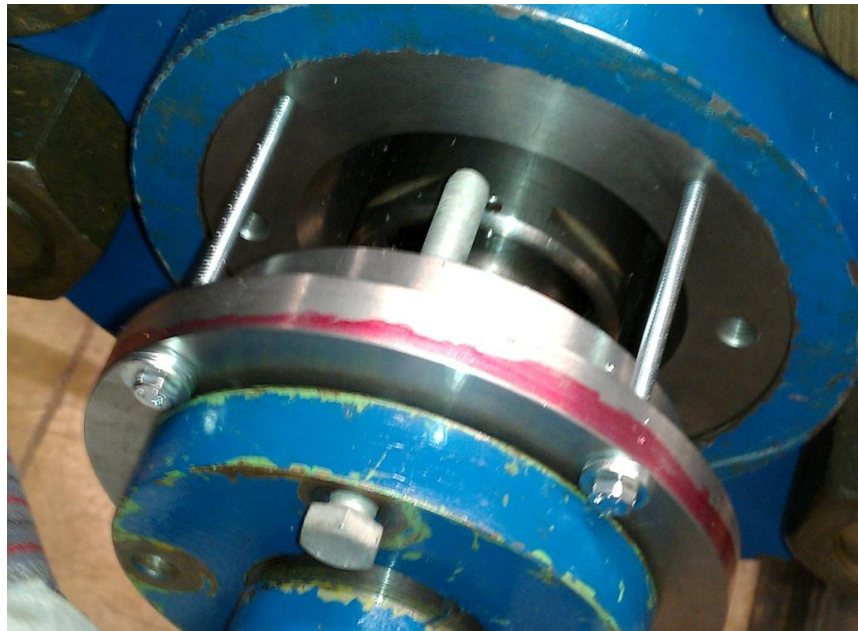

Figure 1.4 Throat locking mechanisms including new stainless steel disk.

CHAPTER 2

TEST PREPARATION DESIGN AND CONSTRUCTION

A significant amount of preparation is required before the test section characterization can begin. These preparations include a relatively simple selection of diaphragm scoring depth, design and manufacture of a system to house and axially translate pressure transducers and heat-flux sensors in the test section, and fabrication of said heat-flux sensors.

2.1 Diaphragm Testing and Selection

Preliminary testing had to be performed to determine a suitable scoring depth on previously available 1008 steel (10 gauge) plates. As this study intends to operate with a P_4 driver pressure of 20.7 MPa (3000 psi) and the double-diaphragm section is kept at half as much pressure, the scoring depth selected should optimally be so that possibility of accidental rupture while pressurizing these sections is minimized while also ensuring that the diaphragms burst cleanly after venting the intermediate double-diaphragm pressure.   These tests were performed on single diaphragms, and the results are shown in Table 2.1. The results show that Test 2 provides the best result, which would result in an anticipated rupture around 3.11 MPa (450 psi) when venting the double-diaphragm section under standard two-diaphragm operation. Test 1 is suitable but would provide fewer margins for error in trying to prevent accidental rupture. Test 3 is completely unsuitable due to the rupture pressure being greater than the intended initial P_4.

Additionally, scoring the diaphragms using a CNC milling machine proved to be the preferred method in minimizing fragmentation or failure of the diaphragm petals by ensuring a uniform depth throughout each cut and consistency between all plates.

Table 2.1 Diaphragm Scoring Test Results

High Pressure Test	Diaphragm Scoring Depth (mm)	Rupture Pressure (MPa)
1	1.016	15.17
2	0.889	17.57
3	0.762	21.03

2.2 Rake and Sting Design

An apparatus must be designed that is capable of securing forward facing pressure transducers across various axial locations in the test section in order to determine the core flow. It must be wide enough to determine the boundary layer of the flow from the expansion nozzle exit to the diffuser at the back of the test section. Additionally, a forward facing probe capable of securing a single thin film RTD sensor must also be incorporated into the design near the axial centerline of the test section (height: $y = 0$; width: $z = 0$) to concurrently measure temperature data.

The above requirements were met by designing two major assemblies, both of which are constructed of multiple parts. One assembly, the rake, was for housing all sensors, and the other, the sting, was a variable length arm for securing the rake in the test section. The conjoint two-assembly system was able to pass all necessary electrical wiring from a vacuum environment to the exterior of the tunnel while shielding them from potential damage during testing.

2.2.1. Rake Design

Previous tests in the HST suggest that the boundary layer of the test section takes up at least 1/3 of the cross-sectional area [4]. Since the nozzle exit diameter is 30.48 cm (12 in.), a rake that spans in both directions from the axial centerline needs to be over 2/3 the length of this diameter, 20.32 cm (8 in.), to ensure that the outermost transducers are within the boundary layer. For simplicity, uniform spacing has been selected, using 9 transducers spaced 2.54 cm (1 in.) apart, with the center transducer laying directly on the axis.

The rake was constructed in two similar top and bottom halves in an effort to make a structure that could house forward facing transducers while still maintaining geometry that could be created through practical machining applications. Simple blocks were machined to directly house and secure the 9 PCB 111A21 transducers selected for the tests. These blocks were then compressed between two corresponding slots in each rake half.

The exterior of the rake was designed to have a circularly rounded leading edge with an arbitrary half angle selection of 3°. This angle was selected primarily to allow a large enough thickness in the rake behind the transducers to create a cavity for passing all electrical wiring to the sensors but was also minimized to keep a low aerodynamic profile suitable for hypersonic testing. Additionally, the transducer blocks were recessed from the leading edge with ports smaller than the diameter of the transducer surfaces to help protect them from flying debris.

On the bottom half of the rake, a bayonet style attachment was created to attach a hemispherical cap for use with the RTD. This probe attachment was designed in accordance to the mounting method used by Kinnear [2]. Components of the probe, including the cap, Teflon sleeve insert, and RTD have all been scaled up to match the scale of the other rake components. Details of the RTD sizing are discussed in Section 2.3.1, and the other components can be seen in Appendix A. Additionally, the leading edge of the hemispherical cap and rake were aligned in the same plane to minimize the possibility of interference by the bow shocks generated from both.

A hollow pipe attachment was also made as a means to attach the rake to the sting while also internally passing the wiring for all ten sensors. The pipe piece has two wings that attach internally at the back of the two rake halves, and the internal pipe diameter was minimized while still allowing enough room for all sensor connectors to be threaded through.

Figure 2.1 shows the general spacing of the sensors in the rake, as well as some exterior dimensions of importance. The bayonet attachment is located directly under the transducer that lies on the test section axial centerline, at $y = -2.54$ cm (-1 in.) and $z = 0$. This is sufficiently close to the centerline to assure measurements are taken in the core flow.
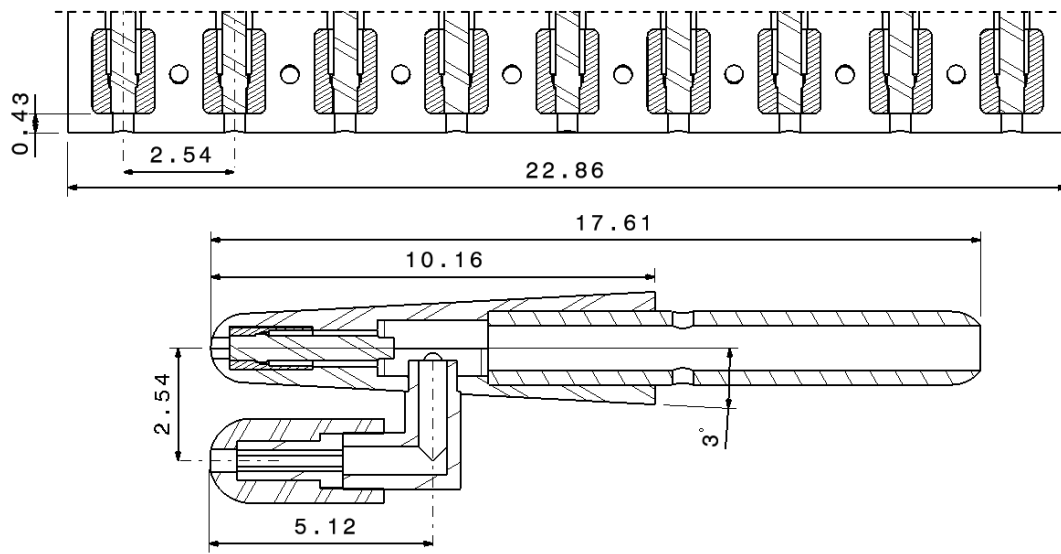
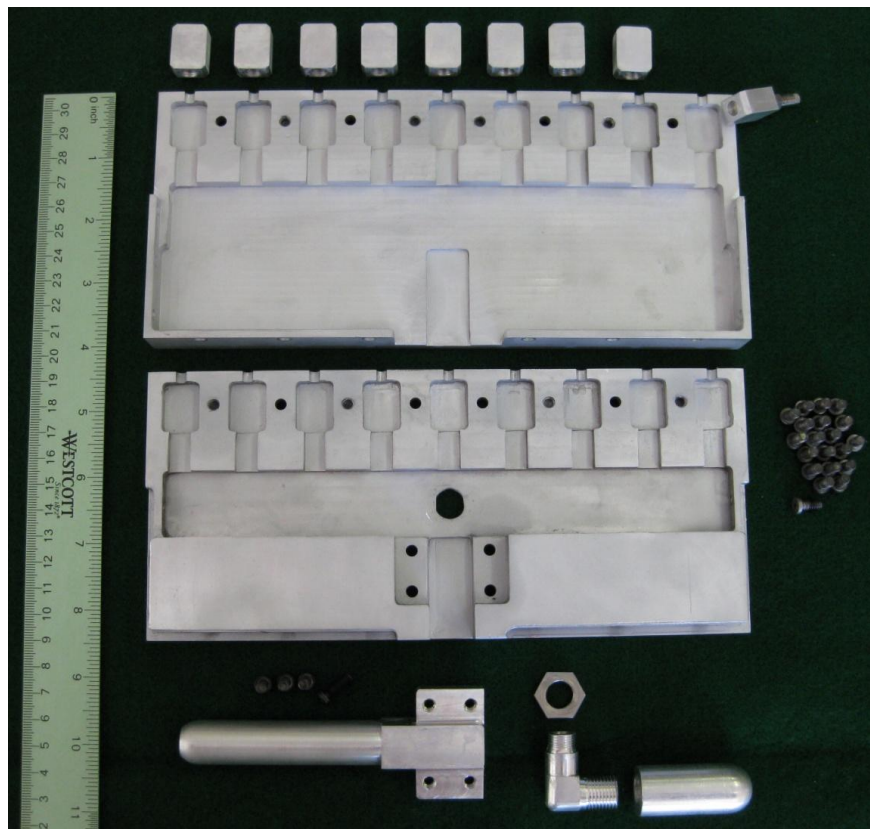11

Figure 2.1 Rake section views (dimensions in cm).

Figure 2.2 Disassembled rake components.

Figure 2.2 shows the disassembled components, including all screws and the flat hexagonal nut used to secure the bayonet attachment to the interior of the rake. All components were made via CNC machining due to the intricacies of the geometry and the need for precisely securing all sensors. Since the exterior durability of the design is a non-factor, 6061 grade aluminum was used to save weight and cost due to the material already being available. Lastly, steel Heli-Coil inserts were used in screw holes near the leading edge to strengthen the threads in the shallow countersunk holes.

2.2.2. Sting Design

The rake assembly needs to be able to be precisely mounted at multiple axial locations in the test section, with the centermost transducer laying on the tunnel centerline. In a concurrent design with the rake, a variable length sting arm was conceived to make use of the newly designed fixed diffuser section just downstream of the test section. The only imposed design restriction was that the outer diameter of the primary sting arm should have a diameter of 5.08 cm (2 in.)

The design process began with a simple flange and insert to match the sizing of the diffuser section ports, which have diameters of 10.16 cm (4 in.) This flange and insert piece was left with a 2.54 cm (1 in.) hole for making a plug or connector for passing wiring through, but the exact means of doing this was left undecided at the time. Additionally, the diffuser ports are radially equidistant from the tunnel centerline with two on top, and one on both sides and the bottom.

With this and the design restriction in mind, a matching set of interlocking pipe fittings were designed for the ends of the primary sting arm and a connector piece that could be attached to the port insert in some manner. These fittings are a simple four petal design that are connected by inserting the matching pieces and then locking by rotating the pipe 45° and securing with screws. This design was selected to create a simple yet secure connection for the sting sections due to the difficulty of installation, as seen in Section 2.4.
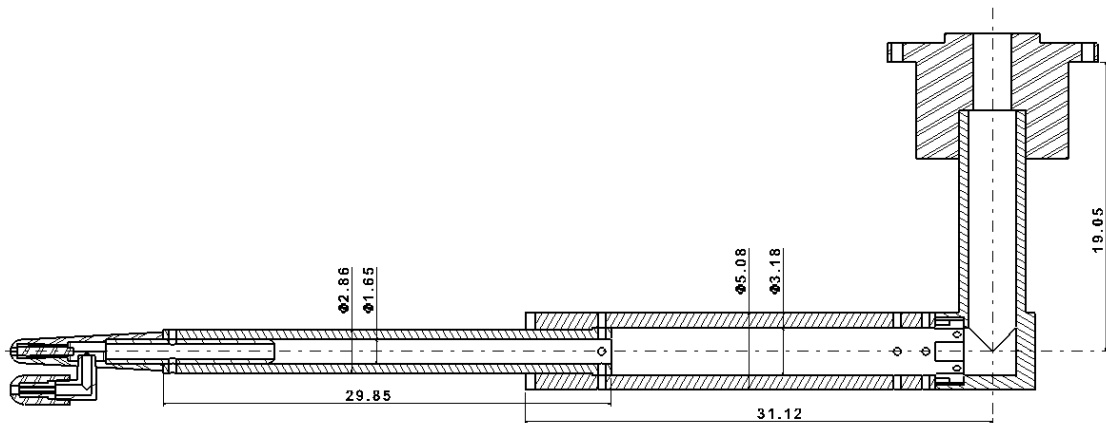
Figure 2.3 Sting section view with attached rake (dimensions in cm.)

Next, a pipe section was selected to connect the port insert and the pipe fitting so that the primary sting arm would lay along the centerline of the test section when all pieces were attached to each other. This was done by over sizing the pipe length and cutting into the side of the fitting piece and port insert to create simple fittings, which were then welded together to make one large sting base piece. This can be seen in Figs. 2.3 and 2.4.

With a basic sting arm now aligned along the tunnel centerline, the length must be decided so that the rake mounted on the end can measure conditions at useful positions in the test section, while also remaining variable length to accomplish this at multiple axial locations. The solution to this was to create a two-section sting which could have its length adjusted by sliding in and out of each other. Since the primary sting arm component outer diameter had been previously established, a secondary smaller diameter sting arm would be made to fit and slide along the interior. This secondary sting arm would also need to have an inner diameter capable of accommodating the rake pipe attachment. Additional outer diameter thickness on the end of the secondary arm and inner diameter thickness on the non-coupling end of the primary arm have been added to create heads which prevent overextension while assembled. The secondary arm also has two half circle slotted groves that run the entire length on each side, and there are corresponding groves in the end of the primary arm. These groves act as a keyway to prevent rotation of the secondary arm. This is done by using short rods as keys

14

between the matching slots in each arm, which are held in place by the interior geometry of the primary arm and a large washer shaped cap on the end. The slots in the secondary arm can then also be used to prevent rotation of the rake attachment, or any device mounted on the end at a future time.

The final part of the general design for the primary and secondary arms involved adjusting the overall length of each one so that the leading edge of the attached rake would be at suitable test locations. The tests were decided to be conducted at three axial locations, with the center test being aligned with the center of the view ports in the test section, and the other two being equal distances from the center test position near the front and back of the test section. Position of the screw holes needed in the primary arm to secure the rake at these locations also influenced the exact positioning of the tests at the front and back of the test section. Ultimately, a combination of port selection between the two top ports on the diffuser and screw hole locations in the primary arm led to the selection of the test locations. Measured from the tunnel nozzle exit, these test locations are at 11.78 cm (4.64 in.), 31.47 cm (12.39 in.), and 51.15 cm (20.14 in.)

An in-depth structural analysis was not performed. Basic calculations showed that the wall thicknesses in each pipe component of the sting design were sufficient in providing a high safety factor even if deflected by the stagnation pressure from the P_5 reflected incident shock conditions in the shock tube. Since the flow undergoes a large expansion process before reaching the test section, the pressure will always be lower in the test section at any given time. Therefore an in-depth analysis was deemed unnecessary.

The full rake and sting assembly is shown in Fig. 2.4. Lastly, since flow downstream of the sensor plane is of no concern, all screws significantly downstream of the leading edge have been designed without countersunk holes in order to simplify the design and installation processes.

Figure 2.4 Assembled sting with rake attachment.

<u>2.3 Thin Film RTD Construction</u>

Fast-response thin film RTD probes must be constructed to measure temperature during the planned low enthalpy test conditions. All RTD construction steps in this section were emulated or modified from the process previously detailed by Kinnear [2]. This includes the same general steps of substrate selection, surface preparation, gauge material application, lead creation, and electrical wiring.

2.3.1. Substrate Selection and Preparation

As demonstrated in previous shock tube experiments, MACOR machinable glass ceramic is an ideal selection for the substrate material of a thin film RTD probe due to its favorable thermal properties, as well as its ease of being machined, which allows for a wide variety of complex geometries. These properties allow the MACOR rods to be heated to 1000 °C (1832 °F) without significant deformation, which is vital during the film application process, and they also provide the insulation required to ensure validity of the semi-infinite substrate

16

thickness necessary for use in the one dimensional theory that governs the experimental results from these thin films.

To match the scaling of the previously designed rake components, 4.76 mm (3/16 in.) diameter and 38.1 mm (1.5 in.) length rods were selected. This length, while excessive in terms of the length needed for the semi-infinite substrate assumption, was selected to ease all phases of construction and testing by having excess material for handling the rods without direct contact with the working surface, film, or leads after their completion.

When applied to the substrate, successful films should result in a thickness of less than 1 μm, and should be smooth and flat without any irregularities. The first step in achieving this is to obtain a finely polished, flat surface on one end of each substrate to be prepared. The process was started by cutting purchased MACOR rods to length with a rapidly rotating abrasive disk using a Dremel-300 series variable speed rotary tool. The polishing was achieved by mounting a series of increasing fine grit sandpaper onto this rotating disk afterwards. 600-grit silicon carbide sandpaper was used to initially polish and round the edges of the working surface. The process was repeated using 1000-grit and 1500-grit sandpaper, until the flat surface and rounds had a visibly polished appearance. Great care was taken in assuring the rounds were smooth and uniform to ensure the possibility of a consistent transition between the gauge material on the end and the lead material on the sides. This was to avoid sharp discontinuities or uneven thicknesses in the film after application, which could result in poor electrical contact between the two materials or even electrical burnout during the calibration or testing processes, destroying the sensor. After the polishing process was completed, the rods were rinsed in water and dried in a clean environment to remove any residual substrate material.

Additionally, since the continuity of the substrate surface is critical to creating functioning sensors, the working surface was examined under a Hitachi S-3000N Variable Pressure Scanning Electron Microscope for imperfections. Figure 2.5 shows a micrograph section of a working substrate surface after completing the polishing process. While not perfect,

it shows what was determined to be an acceptable surface. Note that Figure 2.5 depicts a completed RTD surface taken after the completion of Section 2.3.2, with a portion of the polished surface featured to the right of the film strip. Complications of maintaining a constant film width between RTD samples was circumvented by carefully burnishing one edge of the film. This is seen to the left of the film where the surface is coarser. Surfaces the films lie on are more accurately reflected by the magnified area. Due to the unavailability of a 2000-grit sandpaper and crocus cloth used previously in this construction method, the substrate surface preparation was concluded at this point.
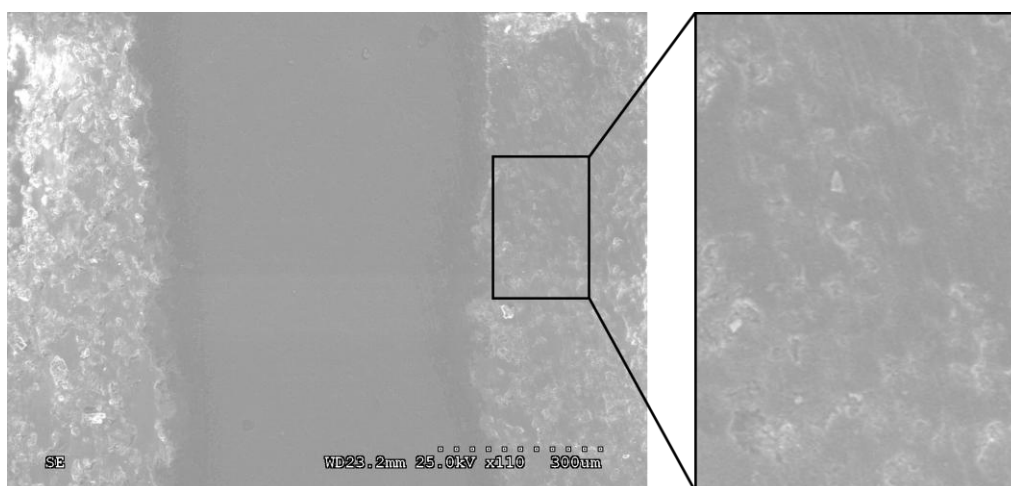

Figure 2.5 Micrograph of a 45 μm section of RTD substrate surface taken at 110x
with 1500-grit polishing.

2.3.2. Film Material Application

After completing the substrate polishing process, the gauge material was applied next. The films are formed through the use of commercially available metallo-organic lusters that are commonly used in ceramic pottery and glass decoration. These metallo-organics are liquid solutions of metallic particles suspended in organic solvents and chemical agents that act as a carrier medium. These additives aid in creating a strong bond between the substrate and the metal and are expelled in a baking process which accomplishes this.

As done with previous testing, platinum was selected due to it being the standard for precision resistance thermometers [2]. "Liquid Bright Platinum R-2" and thinning essence toluene were used to make the films. These were purchased from Standard Ceramic Supply Company located in Carnegie, Pennsylvania. Since film thickness is one of the major factors that determine the sensor's resistance, toluene was used to thin the Liquid Bright Platinum, starting with the previously determined mixture of three parts by volume of thinner to one part Liquid Bright Platinum. In order to create a uniform film on the substrate, a small brush with fine camel hair was used to apply a 1 mm (0.04 in.) wide strip on the working substrate surface with a single stroke. This provided the most consistency in uniform material distribution along the surface, as well as between each substrate rod. The platinum material was immediately dried in an ordinary kitchen toaster oven on a low setting for 10 minutes to prevent contaminates such as dust from mixing with the film material.

To remove the organic carrier from the Liquid Bright Platinum and adhere the metal to the substrate, the ceramic rod samples were placed on a grooved ceramic plate for stability and baked in a Fisher Scientific Isotemp Programmable Muffle 650-Series Furnace. The films were cured by gradually raising the temperature to 765 °C (1409 °F) over one hour and then maintaining at this temperature for an additional thirty minutes. This reveals the need for a durable ceramic substrate that will not deform at such high temperatures, as mentioned in Section 2.3.1. Also, the gradual temperature rise is needed to prevent blistering or boiling of the gauge material. The precise temperature needed to cure the metallo-organic compound is

calculated from the Cone standard [5] for dictating baking duration of glass and ceramics, which is primarily influenced by the heating rate of the furnace or oven being used.

After baking was completed, the rods were left in the furnace overnight to gradually cool. As with the gradually ramp up in temperature to prevent damage to the film material, the temperature also needs to be ramped down gradually to prevent cracking. Cracking in the film can result in the accumulation of stresses, which can ultimately change the resistance of the film during the calibration process when the films are partially reheated and release this stress.

This entire process was repeated with successively less thinning essence to Liquid Bright Platinum ratios until successful films were achieved. Due to the less refined substrate surface achieved in Section 2.3.1, it was found through trial-and-error that the mixture needed to be gradually thickened to achieve continuous films. Ultimately, a 1:1 ratio of thinning essence to Liquid Bright Platinum achieved successful films.

Due to the difficulties of emulating this RTD preparation method, twenty substrate and film samples were prepared per attempt. The successful batch was measured with a Fluke 70 Series II Multimeter and had film resistances ranging from 30-100 Ω, which was determined to be caused by inconsistencies in film thickness and width during application. With three planned tests taken into consideration, five samples of similar resistance were selected from the batch, to allow for possible errors leading up to the completion of the HST tests.

Figure 2.6 shows an identically sized micrograph section of one of the successfully completed RTD films, largely free of inconsistencies or discontinuities. The films are fairly consistent and have sufficient resistance to enable fast response heat transfer measurements. The five sensors, RTD 1 through RTD 5, have resistances ranging between 40-48 Ω and were selected to continue with the process of creating leads from each end of the films and attaching wiring to the leads.
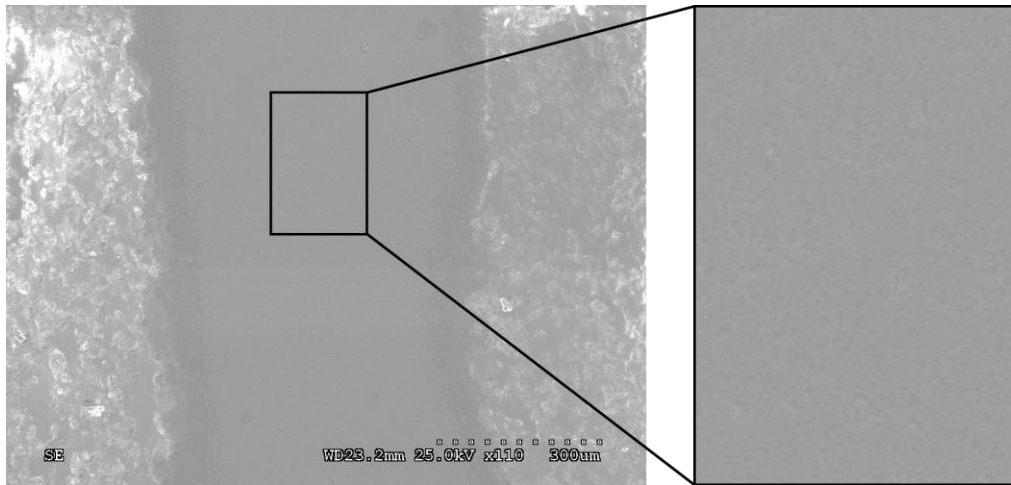
20

Figure 2.6 Micrograph of a 45 μm section of RTD film surface taken at 110x.

2.3.3. Electrical Connections to Film

Electrical leads and wiring need to be connected to the thin films without significantly increasing the diameter of the rods, particularly near the working surface, as the thin film must form a flush and continuous surface with the hemispherical cap to assure that proper stagnation point measurements are recorded. Another metallo-organic solution, "Liquid Bright Gold R-1" from Standard Ceramic Supply Company, was selected for the leads. Gold is a convenient selection for the leads, because it can be applied and cured using the same baking times and temperature used for the platinum films. Gold is additionally suited for used in the leads since it is known to produce continuous thin film connections with other metals such as platinum. Gold has significantly lower electrical resistivity that will prevent it from interfering with readings from the platinum film.

The gold metallo-organic material was applied from the edges of the film to halfway down each rod. It is unnecessary to polish the sides of the rods or dilute the gold material, but the surface must be clean and dry. Attention was taken in assuring the overlap between the gold and platinum interface was kept to a minimum, yet adequate enough to ensure a solid electrical contact. During the calibration and testing processes, it is necessary to subject the

21

RTD to small voltage pulses, as well as lower constant voltage. If the interface between the two films is too small or too thin, electrical burnout could occur when subjected to these voltages, causing the RTD to fail. Adversely, if the gold significantly overlaps the platinum, the film resistance will be reduced by shortening its effective length. After applying the gold material, the samples were dried, baked, and cooled using the same process used for the platinum material.

After assuring that the leads formed successful electrical contacts with the platinum films, the final step was connecting appropriate wire to the gold leads while minimizing the change in profile to the exterior of the ceramic rods. Small gauge uninsulated stranded wire was unwound and attached to the leads at the midpoint of the rods using Pure Silver Conductive Epoxy 8331-14g available from MG Chemicals. The epoxy, which is mixed in two parts and cures gradually with exposure to air, was applied to the connection point between the gold leads and the wire and quickly wrapped with insulating electrical tape to both flatten and secure the connection. Electrical tape was also applied over the gold leads and exposed wiring to electrically isolate the RTD from the metallic hemispherical cap and fortify the delicate lead films and wires from possible damage due to mishandling or installation into the Teflon sleeve used to secure the RTD during testing. After drying, the RTD was again confirmed to have solid electrical contact without raising the resistance by measuring from the newly attached wires.

Figure 2.7 shows a general RTD sketch using this method, as well as an end and side view of a successfully completed RTD used in this particular study. As seen in the end view, the insulating electrical tape is flush with the platinum film plane, which will coincide with the hemispherical cap when installed in the rake bayonet probe. The side view shows that the overall length with excess substrate and wires is about 5 cm (2 in.) Given that the films still have an acceptable range of resistances, the present development shows that the RTDs have been successfully scaled up to match the sizing of the rake.
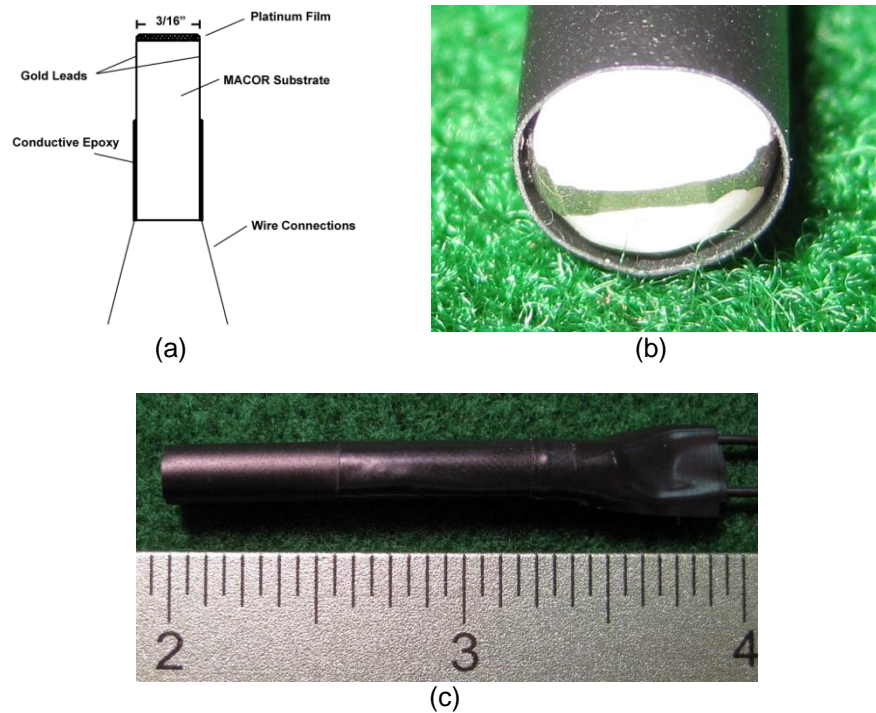
Figure 2.7 Complete RTD. (a) Schematic [2]. (b) End view of film.
(c) Side view.

2.4 Test Apparatus Installation

With completion of all major hardware components of the test apparatus, it needs to be installed to ensure that the intended specification is met, in that it rigidly secures all sensors at the selected test locations. Figure 2.8 shows the assembly mounted in the center of the test section through one of the top ports in the new fixed diffuser section. The sting components and screws used to secure them had to be installed through the other small diffuser ports and test section viewport, which proved to be quite difficult. The simple interlocking mechanism previously designed to connect the base and primary arm proved immensely helpful during installation, as this junction was barely within arm's reach from the test section.

Figure 2.8 Rake and sting assembly installed in HST test section.

While the sting was in its fully extended configuration, the increased moment from its own weight, or any external light force applied to the end, caused the rake to be deflected slightly. To remedy this and fully secure the extended rake, a support structure was added. Shown in Fig. 2.9, two rectangular blocks were cut with matching half circles with the same radius as the outer secondary sting arm radius and secured with bolts on either side. The bottom block was welded to one end of 15.24 cm (6 in.) long turnbuckle, which was secured through a preexisting hole in the bottom of the test section previously used for model mounting purposes. The counter rotating bolt threads on each end of the turnbuckle allowed for the sting to be tightly secured but removed quickly without causing over tightening that could artificially deflect the sting downwards.

Figure 2.9 Turnbuckle support for extended sting.

2.4.1. Wiring and Vacuum Seal

In addition to securing the test apparatus at the desired locations, the necessary wiring must be passed from the sensors, down the sting, and out of the HST test section. Figure 2.10 shows the interior of the rake after wiring has been completed. Due to the possibility of the RTD wiring becoming twisted when connecting the hemispherical cap to the rake, the cap was connected first and then wired in the interior cavity of the rake. Figure 2.10 also shows how the interior cavity dimensions were sized to provide the necessary clearance needed by the circular coaxial connectors used to wire the transducers.

Omega Type-J Insulated Duplex Polyvinyl thermocouple wire was used from the interior cavity to the tunnel exterior for low resistance and durability. Interior edges and corners of the sting geometry were rounded to prevent the stripping of wire casing and the possibility of damaging or cutting the wire itself, and all cables were labeled at each end to assure proper matching was made outside of the tunnel after sealing the interior.
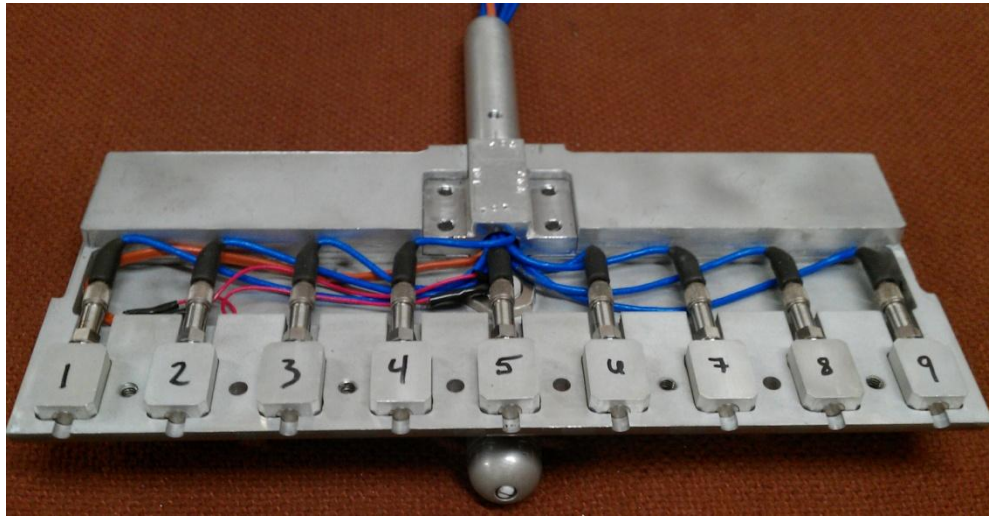
Figure 2.10 Wired rake interior.

Once the wires had passed through the sting base and out of the HST, the previously bypassed problem of creating a vacuum seal had to be addressed. The simplest and most economical solution found was to drill a series of holes through a solid 2.54 cm (1 in.) diameter rubber stopper that matched the wire gauges. The holes were drilled near through the stopper near the outer radius and then had cuts made along its length so that the wires could be radially inserted into the makeshift plug without needing to worry about the sizing of the connectors on either end or having to thread the long lengths of wire through a central hole. After adjusting the plug location along the length of the wires to suit the lengths needed for each individual test, the plug was gently hammered into the opening of the sting port flange and sealed with RTV silicone. The silicone, which typically takes a full day to completely cure, was deemed solid enough for testing just a couple of hours after application due to the low pressure difference between the interior and exterior of the test section. With a maximum differential of one atmosphere, the semi-cured silicone proved more than enough in creating a vacuum tight seal. Due to a new RTD needing to be wired for each test, this seal had to be removed each time as well, and with an already lengthy test preparation time, being able to vacuum the test section and operate the tunnel with this condition helped expedite testing by a considerable amount.

Figure 2.11 shows the simple rubber stopper's effectiveness in creating a seal after passing ten wires between the two distinct environments.
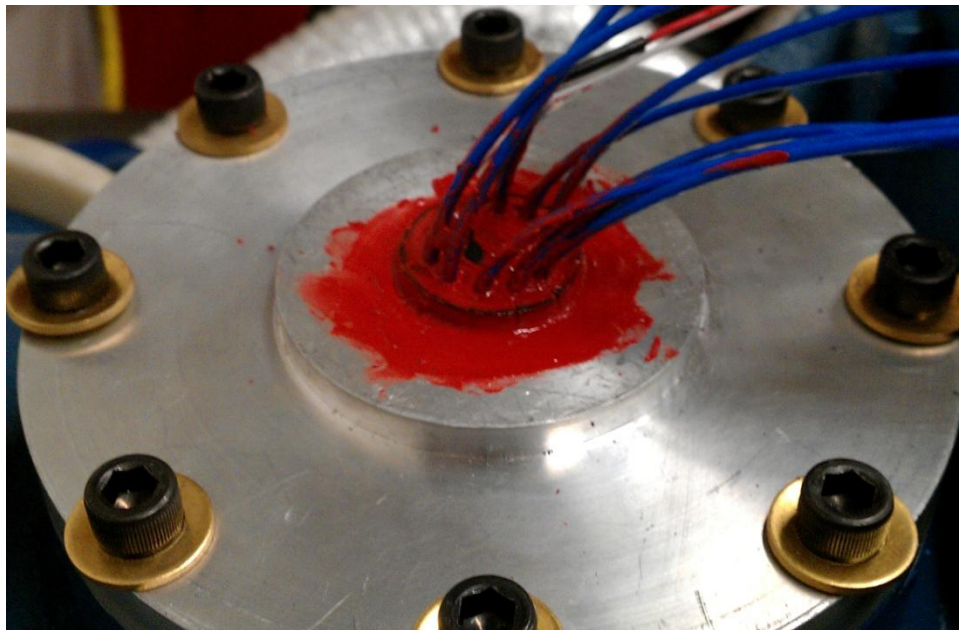

Figure 2.11 Wiring threaded through rubber cork and sealed with RTV silicone.

CHAPTER 3

THIN FILM RTD CALIBRATION

In order to convert electrical voltage output from the RTDs into useful temperature and heat flux measurements, two key thermal properties of each probe must be determined experimentally through calibration testing [2]. These properties are the temperature coefficient of resistance, α_R, and the thermal product, $\beta = (\rho c k)^{1/2}$. They can be determined from static and dynamic calibrations tests, respectively.

3.1 Static Calibration

Ideally, the resistance of the thin film is linearly proportional to the temperature it experiences. The temperature coefficient of resistance depends on a multitude of factors, such as the material selected and the geometry of the film, and the useful linear range is dependent on the uniformity and purity of the metal, as well as its adherence to the substrate. Since these factors could not be replicated perfectly in a precisely controlled manufacturing process, much less by hand, each RTD must be calibrated independently.

The sensitivity and linearity of this relationship can be determined for each sensor by using a liquid medium to heat the RTD, which allows the film resistance to be measured at various temperatures. The RTDs were individually immersed in a glass beaker containing 99.5% glycerin $C_3H_5(OH)_3$ and placed on a hot plate. Glycerin was selected as a medium due to its high boiling point and low gas solubility since the presence of gases could complicate interpretation of the results. The increased temperature range provided by the glycerin allows for measurements up to it boiling point, 290 °C (554 °F.) However, calibration for this study was only performed from ambient conditions to 120 °C (248 °F,) as this range adequately covers the expected temperature rises in the planned HST tests.

28

A scientific glass mercury thermometer was used with a Fluke 70 Series II Multimeter to calibrate each probe. Through experience, this was most easily accomplished by wiring the RTDs into a circuit with the multimeter to actively monitor the resistance while preheating the glycerin above the measurement range and then recording readings as it gradually cooled. This method was determined to minimize errors in data collection to the accuracies of the thermometer and multimeter.

Performing a least-squares linear regression on the data reveals the slope of the resistance-temperature correlation, $\Delta R/\Delta T$, which can then be used to determine the temperature coefficient of resistance via the relationship

$$\alpha_R = \frac{1}{R_0}\frac{\Delta R}{\Delta T} \tag{3.1}$$

where R_0 is the resistance of the film at the ambient temperature of the actual testing process. If the ambient temperature of the calibration and actual test conditions differ and are not taken into consideration, the resulting heat flux calculation will have an approximate 1% error increase for every 5 to 10 K difference [2].

3.2 Dynamic Calibration

After completion of the static calibration, a dynamic calibration needs to be performed to determine the thermal product of each RTD. As with the thermal coefficient of resistance, the thermal product depends heavily on the history of the gauge construction. In particular, it depends on the substrate surface preparation and even the firing details of the ceramic production process [2]. Due to the interpenetration of platinum and ceramic that occurs at the interface between the films and substrates, the physical properties ρ, c, and k that determine the thermal product, are not the properties of the bulk material and cannot be measured directly. Therefore, a transient double electrical discharge calibration method was employed to experimentally determine each thermal product.

R1 = R3 = R4 = 50 ohms   Vi = Input Voltage

RL = Lead/Wire Resistance   Vo = Output Voltage
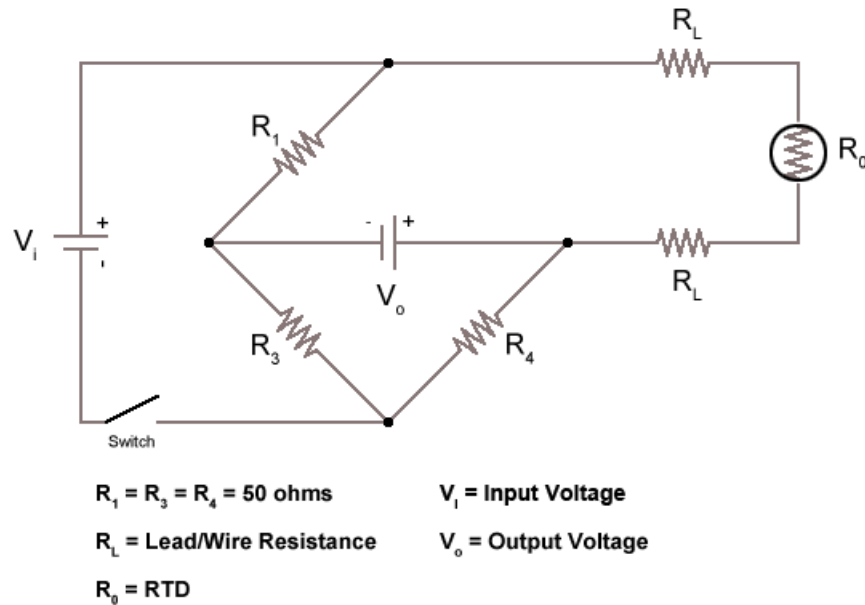
R0 = RTD

Figure 3.1 Wheatstone bridge circuit diagram used for calibration and testing.

Each RTD was incorporated into the Wheatstone bridge circuit shown in Figure 3.1 and supplied with an approximate 0.1 ms, 10 V rectangular voltage pulse using a DVIII DC Transistor Power Supply and a simple button switch to briefly close the circuit. This pulse causes ohmic heating in the film, which causes a change in resistance. Excessive pulse duration or repetition should be avoided as exceedingly high film temperatures can cause the connections between the platinum and gold or the gold and silver epoxy to fail. Ideally, the pulse magnitude and duration should be selected in order to heat the film enough to achieve the desired bridge output, but not enough to cause damage to the film through repeated or prolonged exposure. It is wise to monitor the film or lead temperatures after each pulse to ensure the delicate probe metals remain as close to the ambient temperature as possible, to avoid possible damage from overheating. The pulse was initiated by the simple button switch for all dynamic calibration tests. The change in resistance is then recorded as a voltage output across the bridge circuit by a Tektronix DPO 4054 Digital Phosphor Oscilloscope, and it is equivalent to the temperature-time history of the gauge. Additionally, for a constant heat transfer rate to the surface, it has been shown previously that this temperature change is

directly proportional to the square root of time [2]. This relationship can be utilized to closely determine the thermal product of each RTD in a method similar to the static calibration used to determine the thermal coefficient of resistance.

The first half of the test was conducted in air, where heat loss from the film to the surroundings was negligible in comparison to the heat conduction to the substrate. Plotting the voltage response of the first few milliseconds as a function of the square root of time ideally produces a linear response, which can then be fit with a least-squares linear regression to determine the slope that best fits the slope of the data. The test was then repeated with the same conditions with the exception of the RTD being immersed in glycerin $C_3H_5(OH)_3$, where a small but more significant fraction of heat was dissipated into the fluid as opposed to the substrate. This manifests as a temperature-time curve with the same general shape as the air test only with a smaller output voltage. Also plotting this output as a function of the square root of time and fitting a least-squares linear regression to the data will determine the second slope approximation needed to calculate the thermal product.

Figure 3.2 shows the bridge circuit used to conduct this calibration, as well as the experimental program later in the HST. The top left shows the circuit constructed on a breadboard with three identical resistors near the range of resistance exhibited in the RTDs. The top right shows the connection to the DC power supply via alligator clips, with the button switch for triggering rectangular voltage pulses incorporated between the negative terminals. The bottom left shows two more clips that connect the output to the digital oscilloscope, and the bottom right shows one of the RTD probes submerged in a beaker containing ambient temperature glycerin for a test.
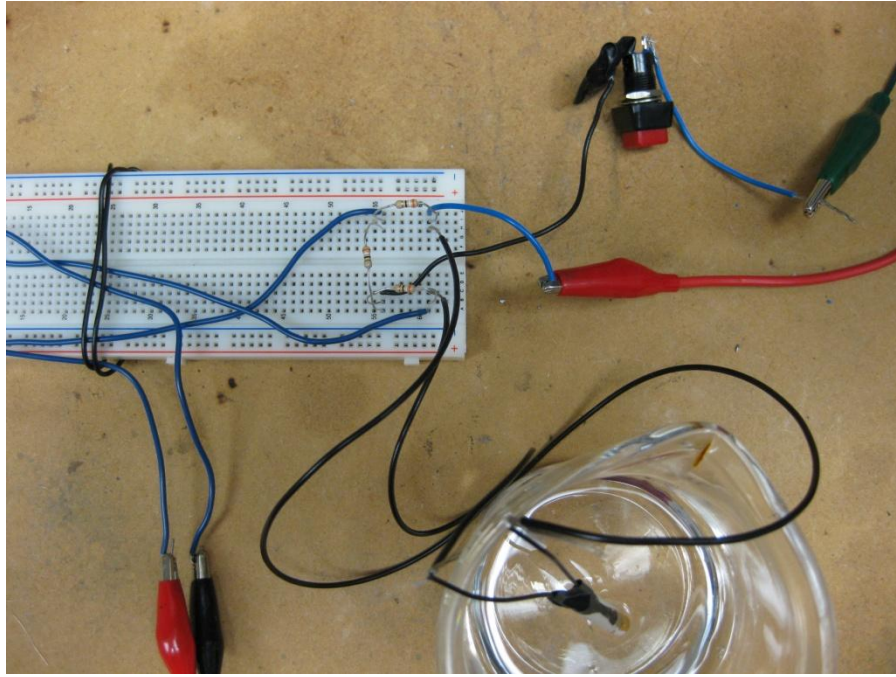
Figure 3.2 Circuit with RTD immersed in glycerin beaker for dynamic calibration.

The ratio of the two slopes determined from the square root of time least-squares linear regressions can then be used to calculate the thermal product from the relationship

$$\beta = \frac{\beta_{gly}}{\dfrac{(\Delta V/\sqrt{t})_{air}}{(\Delta V/\sqrt{t})_{gly}} - 1} \tag{3.2}$$

where the thermal product of glycerin $C_3H_5(OH)_3$ is given as 0.0933 $J/cm^2/K/s^{0.5}$ [6].

Using the Wheatstone bridge in this setup with three constant resistors and one varying RTD resistance causes it to be unbalanced. This imbalance appears as a step input indicating an infinite heat transfer rate at the start of the test. One remedy is to replace one of the resistors with a potentiometer and finely balance the bridge by repeatedly conducting the voltage pulse and making adjustments until the step output is removed. However, this is a troublesome approach considering the delicate nature of the micro-scale thin films. It should be noted that the first of the selected five RTDs was destroyed from electrical burnout during its dynamic calibration by exposing it to repeat voltage pulses too quickly, causing the film to

overheat and fail.   A simple alternative, as discovered through experience, was to simply translate the data afterwards to a balanced output.   Results from the calibration process showed that the temperature-time history of the RTDs after the step output still adhered to the known square root of time relation, and therefore could be similarly applied to determine the thermal products of the remaining probes while minimizing their exposure to the voltage pulses need to conduct the calibration.

Additionally, care was taken to make the circuit as inductance free as possible.   If induction occurs, it will appear as a small oscillation in the temperature-time curve. Sources of interference include coiling or wrapping of uninsulated wire that can produce magnetic fields, as well as domestic sources of electromagnetic waves such as cell phones and radios.

CHAPTER 4

EXPERIMENTAL PROGRAM

Experiments were performed in the HST to characterize the test section under low enthalpy conditions using a newly designed rake and sting housing system to measure pressure and temperature with commercially available transducers and proven thin-film RTD concepts respectively. These measurements were taken at three equidistant axial locations in the test section and were designed to reveal flow characteristics that are useful for planning future experiments using similar conditions. Variance in the testing procedure was kept to a minimum between each test aside from the axial measurement location.

The tests were performed using the diaphragms selected in Section 2.1 with upstream P_4 driver pressures of 20.7 MPa (3000 psi,) initial P_1 driven pressures of 0.102 MPa (14.8 psi,) and test section back pressures between 0.0042 and 0.0044 MPa (0.61 and 0.64 psi.) All tests were conducted using dried air at ambient temperatures of approximately 22 °C (71.6 °F,). A Mach 10 nozzle was used for the tests.

4.1 Shock Tube

Even with careful preparation, each test will inadvertently have variation in the observed flow properties in the shock tube, at the throat, and in the test section due to imprecise replications of diaphragms, pressures, ambient temperature, or a multitude of other variables. Therefore, it is necessary to document various properties for each case to properly quantify the flow upstream of the test section.

In addition to this, previous shock tube experiments show that theoretically computed shock strengths are higher than those in actual tests from the shock decelerating as it travels down the tube, due to boundary layer growth. The relative position of this contact surface to the incident shock can be seen in Figure 1.3.

Due to these complications, the shock speed must be physically measured for each test, making it unnecessary to precisely measure the P_4 driver or double-diaphragm section pressures. These readings should be taken as close to the end as possible in order to minimize any discrepancy between the measured shock speed and the actual speed at the throat. Two PCB 111A23 pressure transducers were used at Stations 5 and 6 in the driven section near the throat, which are precisely 137.16 cm (54 in.) apart [1]. From the distance and time of the shock passage from the data, the Mach number can then be computed from

$$M_s = \frac{u_s}{a_1} = \frac{\left(x/\Delta t\right)}{\sqrt{\gamma_1 R_{g,1} T_1}}$$

(4.1)

where the velocity u_s is computed from x, the distance between the transducers, and Δt, the lapsed time between the initially recorded signals, and the ambient speed of sound a_1 being calculated from γ, R_g, and T, the specific heat ratio, gas constant of air, and temperature ahead of the incident shock, the subscript 1 referring to the conditions ahead of the shock.

From the calculated normal shock, it is possible to obtain the stagnation conditions at the throat. The desired total conditions, pressure, density, temperature, and enthalpy, P_t, ρ_t, T_t, and H_t respectively, can be determined through a series of cumbersome calculations by finding the stage 5 conditions behind the reflected incident shock. As an alternative, a more expedient method was employed by using NASA's Chemical Equilibrium with Applications (CEA) code for solving reflected incident shock tube problems [7]. Frozen flow calculations were used due to the shock strength being low enough to cause minimal disassociation of gases. Calculations using equilibrium conditions confirmed this, as only a negligible change in stagnation properties occurred between the two states.

Even though the nozzle is designed for Mach 10, boundary layer growth causes the actual freestream Mach to be lower. Using the calculated specific heat ratio behind the reflected incident shock and the measured throat to nozzle exit area ratio, the freestream Mach number can be back solved with a numerical solver using the area-Mach relation [8]

$$\left(\frac{A}{A^*}\right)^2 = \frac{1}{M_\infty^2}\left[\frac{2}{\gamma_5 + 1}\left(1 + \frac{(\gamma_5 - 1)}{2}M_\infty^2\right)\right]^{(\gamma_5+1)/(\gamma_5-1)} \tag{4.2}$$

Other freestream conditions at the nozzle exit can then be calculated using the stagnation conditions and newly calculated freestream Mach numbers with the isentropic relations

$$\frac{T_t}{T_\infty} = 1 + \frac{\gamma_5 - 1}{2}M_\infty^2 \tag{4.3a}$$

$$\frac{P_t}{P_\infty} = \left(1 + \frac{\gamma_5 - 1}{2}M_\infty^2\right)^{\gamma_5/(\gamma_5-1)} \tag{4.3b}$$

and

$$\frac{\rho_t}{\rho_\infty} = \left(1 + \frac{\gamma_5 - 1}{2}M_\infty^2\right)^{1/(\gamma_5-1)} \tag{4.3c}$$

The Reynolds number is another useful property for understanding the freestream flow conditions. It is typical to quote the Reynolds number by its value per unit length. This can be calculated by [9]

$$Re_\infty/x = \frac{\rho_\infty u_\infty}{\mu_\infty} \tag{4.4}$$

where the dynamic viscosity μ_∞ is calculated from the well-known Sutherland's Law

$$\mu_\infty = \mu_{ref}\left(\frac{T_\infty}{T_{ref}}\right)^{3/2}\frac{T_{ref} + s}{T_\infty + s} \tag{4.5}$$

with the reference conditions $s = 110.4$ K, $T_{ref} = 273.15$ K, and $\mu_{ref} = 1.716 * 10^{-5}$ kg/(m s) for air. These cumulative conditions should now thoroughly quantify the flow upstream of the test section for each run.

4.2 Test Section

Now that the flow conditions entering the test section have been properly tabulated, the primary interests of the tests can be focused on. This includes using the average measured pressure readings to create a pressure and Mach distribution profile at the selected axial test locations, tracing the approximate useful core flow from this data along with calculated oblique shocks and expansion waves, and determining useful heat properties near the axial centerline

at those same locations, including the increase in stagnation temperature and the approximate heat transfer rate, or heat flux, $\dot{q}$.

4.2.1. Transducer Analysis

Regardless of axial position or relative position to the core flow across any cross section, the Pitot signal outputs from shock passage in the test section generally have the same characteristic record. A strong voltage impulse is observed as the shock makes initial contact and forms a bow shock in front of the leading edge. This transient spike is then quickly damped into a quasi-steady state immediately behind the shock. This continues for a short variable length of time until the flow begins to destabilize or is interrupted by the driver gas arrival. This quasi-steady flow behind the shock is the output range of interest needed to quantify a local total pressure [10].

Due to high sampling rates and sensitivities, the raw data contains a lot of noise and sharp discontinuities that may interfere with determining an accurate pressure reading. To remedy this, a low-pass Butterworth filter was used to lightly filter the data by removing excessively high frequencies from the response. This filter also results in maximum possible amplitude smoothness, helping to remove the discontinuities, sharp variations, and other irregularities. Figure 4.1 demonstrates the filter's effectiveness in smoothing the response without removing potentially useful data by removing frequencies above 20 kHz.
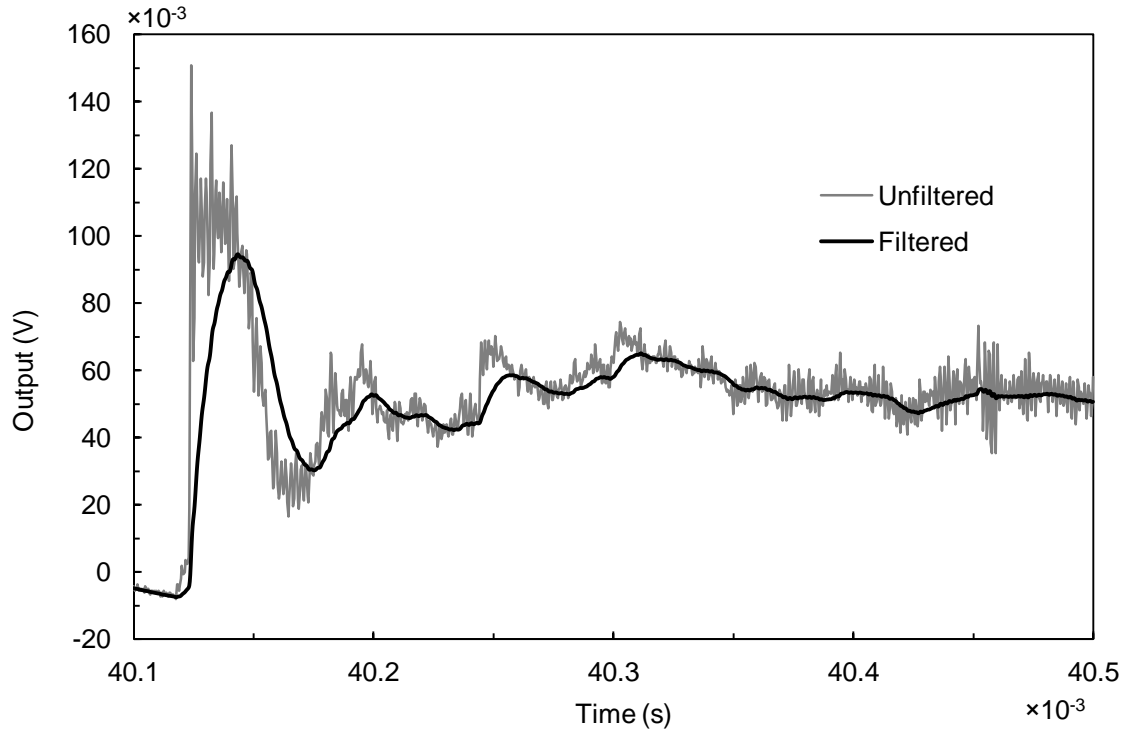
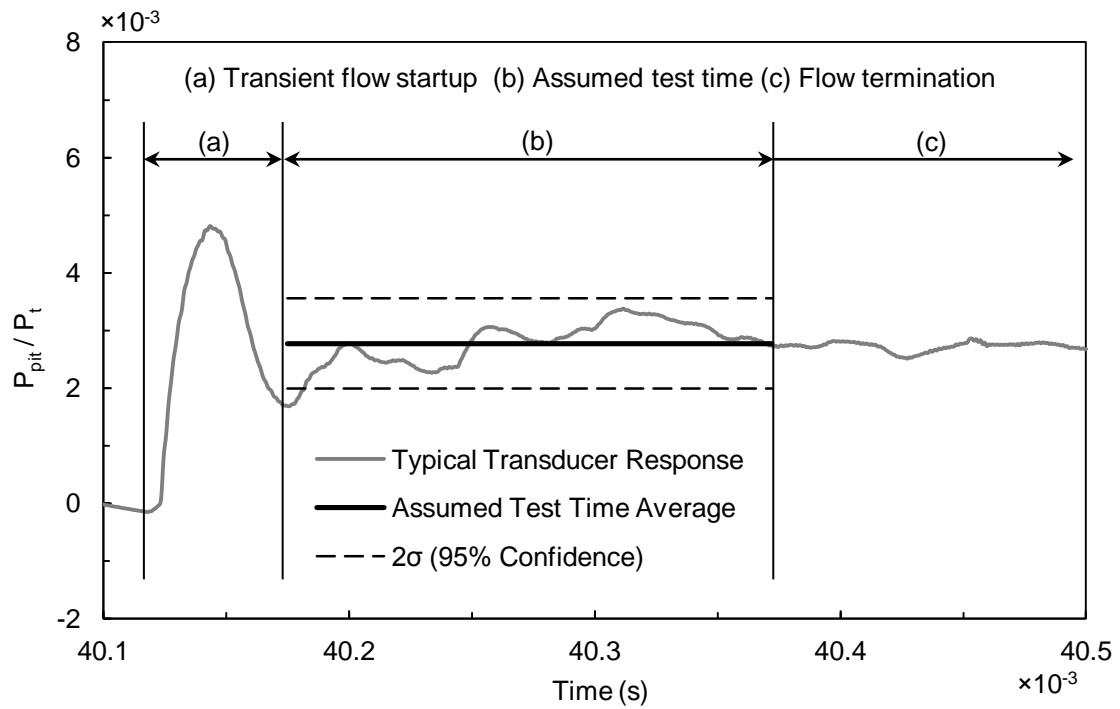Figure 4.1 Typical Pitot pressure transducer response

Figure 4.2 Pitot pressure sample analysis

Figure 4.2 shows a typical filtered result with the three expected stages observable with any given transducer response. As this method is trying to assign a static value to a dynamic signal there is a degree of variance between the results of a given signal, even if the flow conditions are assumed to be similar. Due to this, the assumed useful test duration must be carefully considered by taking all nine concurrent readings into consideration, with some variability between the inferred core flow and boundary layers. In general, the duration of the test time is governed by the shock strength, uniformity of the flow, and the tunnel back pressure in front of the shock.

For this study, the average of the measured test time, excluding data beyond two standard deviations, was converted to a useful pressure measurement using the manufacturer supplied sensitivity, which was 51±1 mV/psi. These values can be plotted versus their location to reveal the general pressure profile at each test plane, but it is more apt create a non-dimensional scale by normalizing these values with respect to the stagnation temperature, P_t, since this affords some consistency between test results where the runs have varying upstream flow characteristics.

These pressures can also be converted directly to the local freestream Mach numbers to express the distribution in an easily understood format. This can be done by using previously determined conditions with the Rayleigh-Pitot formula [11] and numerically solving for the Mach number:

$$P_{\text{pit}} = P_\infty \left[\frac{(\gamma_5 + 1)M_\infty^2}{2} \right]^{\frac{\gamma_5+1}{\gamma_5-1}} \left[\frac{\gamma_5 + 1}{2\gamma_5 M_\infty^2 - (\gamma_5 - 1)} \right]^{\frac{1}{\gamma_5-1}} \tag{4.6}$$

For the core flow, these calculated Mach values should closely approach but not exceed the calculated freestream Mach number entering the test section, and they will decrease with proximity to the wall due to the boundary layer.

4.2.2. RTD Analysis

The measured RTD output resembles the temperature-time curve observed in the dynamic calibration for the first few milliseconds after the initial shock passes, followed by a rapid increase as the driver gas arrives. The useful test time varies between each test and is limited to time between the initial shock passage and the arrival of the driver gas. Only the initial square root of time relation in the response during this timeframe is useful for characterizing the flow. This time was experimentally shown to decrease as the distance from the expanding nozzle exit increased. Calculated heat transfer rates were limited to a maximum of one millisecond for this study. The delicate and unprotected thin films were destroyed by the arrival of the high-pressure driver gas, so the sensor must be replaced with a new one for each test.

A Wheatstone bridge deflection method can be used to convert the time-varying voltage signal to useful temperature measurement with the relation [12]

$$\frac{V_o + \Delta V_o}{V_i} = \frac{R_1}{R_1 + R_0'} - \frac{R_3}{R_3 + R_4} \tag{4.7a}$$

where the initial input is the constant voltage supplied to the bridge during testing, the voltage output and initial resistances are all measured quantities, and

$$R_0' = R_0 + \Delta R_0 \tag{4.7b}$$

signifies the change in the RTD film resistance when subjected to a change in temperature. Solving equation (4.6a) and equation (4.6b) for $\Delta R/\Delta V$ and dividing by the previously determined RTD sensitivities $\Delta R/\Delta T$ from equation (3.1) yields the desired conversion factor.

Next, the stagnation point heat transfer rates must be determined using two techniques that require the thermal properties determined from the RTD calibrations, the temperature coefficient of resistance and the thermal product.

The first method works under an ideal one-dimensional heat flux assumption where the voltage output perfectly conforms to the temperature-time relation. This constant heat flux case can be represented by the relationship [2]

$$\dot{q}_s = \left(\frac{\rho c k}{t}\right)^{1/2} \frac{\pi^{1/2}}{2} \frac{\Delta V}{\alpha_R V_o}$$ (4.8)

which can be simplified with some simple substitutions. Plotting the useful data range of the response versus the square root of time allows for a least-squares linear regression to be generated, which has the general form

$$\Delta V = \lambda \sqrt{t} + c$$ (4.9)

where λ is the slope and c is a constant caused by any initial offset. As previously mentioned, any impulse in the response caused by an initially imbalanced bridge can be removed by translating the square root of time portion of the relation to remove the offset. The data can then be translated with respect to time to remove any offset in the regression line ($c = 0$.) Substituting equation (4.9) into equation (4.8) and replacing the thermal product terms yields a form that can be used to directly calculate the constant heat flux.

$$\dot{q}_s = \frac{\beta \sqrt{\pi}}{2\alpha_R V_o} \lambda$$ (4.10)

The second method was a numerical technique for calculating heat flux under non-constant heat transfer conditions. The Cook-Felderman algorithm is a piecewise linear expression that approximates heat flux using the already uniformly discretized data points. Since this method contains no integration approximations, its accuracy is only limited by the degree to which the true heat flux is approximated by the voltage response and to the degree the voltage response is approximated by the function. The algorithm is [13]

$$\dot{q}_n(t) = \frac{\beta}{\sqrt{\pi}\alpha_R V_o} \left[\frac{V(t_n)}{\sqrt{t_n}} + \sum_{i=1}^{n-1} \left\{ \frac{V(t_n) - V(t_i)}{\sqrt{t_n - t_i}} - \frac{V(t_n) - V(t_{i-1})}{\sqrt{t_n - t_{i-1}}} \right. \right.$$

$$\left. \left. + 2\frac{V(t_i) - V(t_{i-1})}{\sqrt{t_n - t_i} + \sqrt{t_n - t_{i-1}}} \right\} + \frac{V(t_n) - V(t_{n-1})}{\sqrt{\Delta t}} \right]$$ (4.11)

41

where n is the equally divided number of points by time Δt and t ranges from 0 to $n\Delta t$. Due to the instability of the algorithm, previous work [2] and experience show that the raw RTD response cannot be used directly due to sharp fluctuations caused by noise. These fluctuations cause large errors in the calculated heat flux. The solution found was to approximate the data by determining a least-squares linear regression on the data, plotted with respect to the square root of time in an identical procedure as the one used in the constant heat flux case, and then plotting the regression back in the normal time domain to create a smooth parabolic fit to represent the temperature-time curve. Due to its unstable nature, the Cook-Felderman algorithm quickly converges on the approximate heat flux value but also diverges quickly near the end of the sequence in an undamped oscillatory manner. This is of no concern, and the divergence can be truncated to reveal a near constant solution.

4.3 Data Collection

The RTD wired from the test section was incorporated into the same Wheatstone bridge as depicted in Figure 3.1, with the output monitored by one of the four channels of the Tektronix DPO 4054 Digital Phosphor Oscilloscope and with the switch removed. The bridge was given a constant excitation of 4 V from a DVIII DC Transistor Power Supply. An additional two channels on the digital oscilloscope were used to measure the normal shock passage just upstream of the throat using the two PCB 111A23 pressure transducers.

Nine additional channels were needed to record Pitot data from the nine PCB 111A21 pressure transducers located in the test section. This was accomplished using two National Instruments TB-2709 DAQ cards with a NI PXIe-8130 Embedded Controller and processed by NI LabVIEW software. The general length of the useful test time data varied with location relevant to the boundary layer and core flows, as well as axial location, and was observed to range from 50 to 200 μs for the given test conditions and locations.

All pressure transducers were supplied power from a PCB model 483A signal conditioner, and all input channels on the oscilloscope and DAQ system were captured using a 25 MS/s sampling rate over a range from upstream of the initial shock tube transducer to downstream of the test section. This was determined to be an adequate frequency for the Pitot data, and more than adequate for the RTD and shock tube transducer data. Recordings were triggered by an internal triggering function of the digital oscilloscope using the initial shock tube transducer, which is initiated by the measured voltage exceeding a used defined limit. This triggered both the recording on the oscilloscope and a rectangular output voltage pulse that was used to trigger the DAQ system recording. From this, a sufficient timeframe upstream and downstream of the trigger points was recorded to capture all necessary data.

CHAPTER 5

RESULTS AND DISCUSSION

Specific test results are discussed in this chapter, including the RTD static and dynamic calibration processes, the shock tube test conditions, Pitot pressure transducer response processing, and RTD heat flux calculations.

5.1 RTD Calibration

Five thin film RTD sensors were selected from a batch of samples constructed in an iterative construction process similar to those used in previous experiments [2]. Due to difficulties in the replication process, including substrate preparation and an inability to finely regulate the thickness and consistency of the platinum films, resulting resistances spanned a wide range and were lower than expected. The five selected do not necessarily have the highest resistances, but rather they are the five from the last successful batch with the most similar resistances, which ranged between 41-48 Ω. This was done in an attempt to minimize one degree of variability expected with the test results. Two of the selected five did not survive the calibrations and test setup in their entirety before being able to be used for data collection in the HST test section. Furthermore, the harsh testing environment thoroughly destroyed the remaining three sensors after a single test each by erosion of the entire film surface.
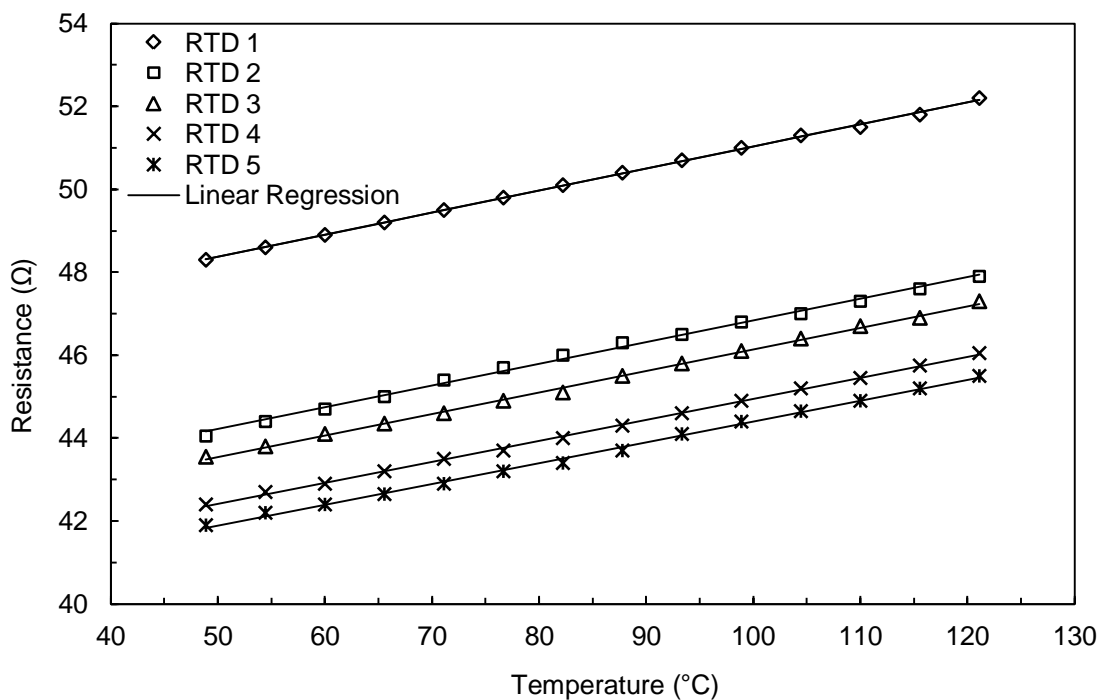
Figure 5.1 Static Calibration of RTDs.

5.1.1. Static Calibration

Figure 5.1 shows the static calibration results for the selected RTDs. Data points were collected at set intervals by carefully controlling the cooling rate of the glycerin $C_3H_5(OH)_3$ used as a medium to heat the platinum films. The sensitivities were determined by the slope of least-squares linear regression fits for each data set. Each regression was found to be highly accurate, with correlation coefficients exceeding 0.995. Correlation of the data was limited by the accuracy of the timing used to record readings at each specified temperature as the medium cooled and by the resolution of the instruments used to collect the data.

Pertinent results of the static calibration are tabulated in Table 5.1. This includes the sensitivities discovered from the linear regression slopes, the regression correlations to the actual data, the temperature coefficients of resistance, the approximate measured resistance values at 25 °C (77 °F,) and the error analysis. The temperature coefficients of resistance were calculated using the sensitivities and the ambient test temperature.

Table 5.1 Static Calibration Results

RTD	R at 25 °C	α_R (K^{-1})	± Percent Error	Sensitivity (Ω/°C)	Correlation Coefficient
1	47.9	0.00111	0.96	0.0532	0.9994
2	43.2	0.00121	1.29	0.0524	0.9967
3	42.7	0.00122	1.33	0.0519	0.9983
4	41.3	0.00123	0.84	0.0506	0.9991
5	40.9	0.00123	1.44	0.0502	0.9977

Due to the expected linear relationship between resistance and temperature, the linearity of the data is of importance and was the primary factor used in calculating the percent error. Hysteresis error was discounted as being negligible due to the slow and controlled cooling rate of the medium and the careful measurements at each temperature.

5.1.2. Dynamic Calibration

Electrical discharge calibrations were performed using a Wheatstone bridge to determine the thermal products of each RTD. A rectangular voltage pulse varying from 10-12 V was supplied to the circuit to create appreciable ohmic heating in the platinum thin films, causing varying responses when exposed to air and glycerin. Using an initially unbalanced bridge circuit resulted in an initial step in output voltage that did not affect the curvature of the data needed for calibration, which should ideally be proportional to the square root of time. Figure 5.2 shows superimposed results of a typical RTD response after removing the initial step from the imbalanced bridge.
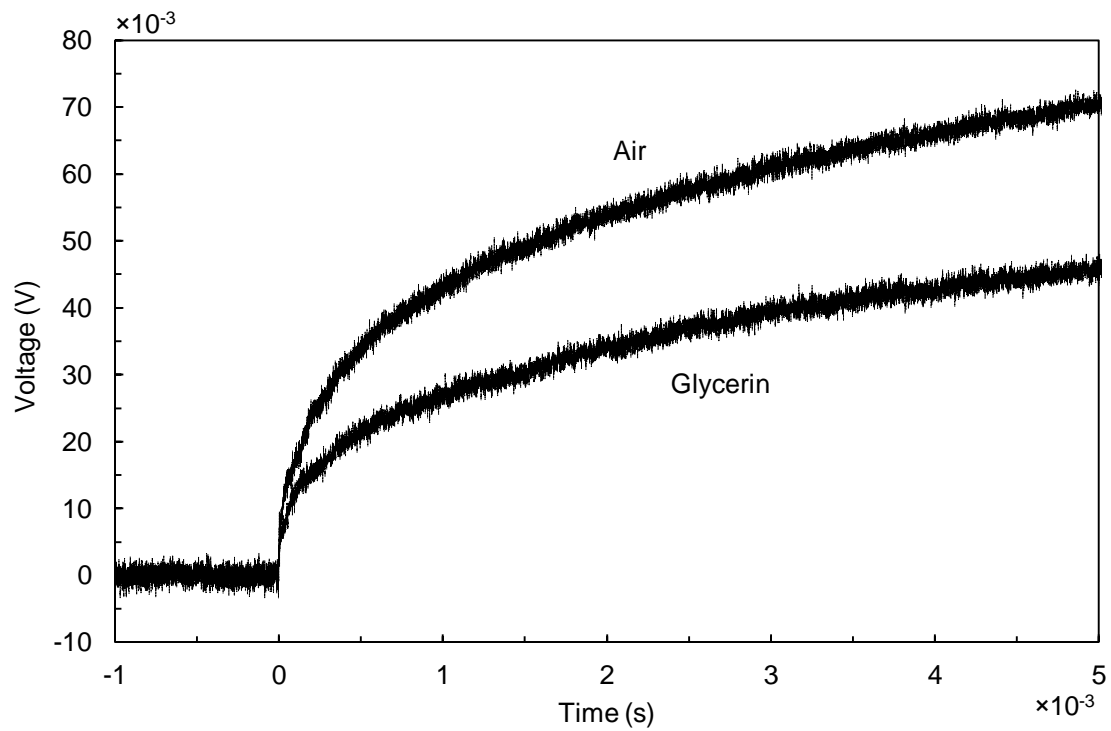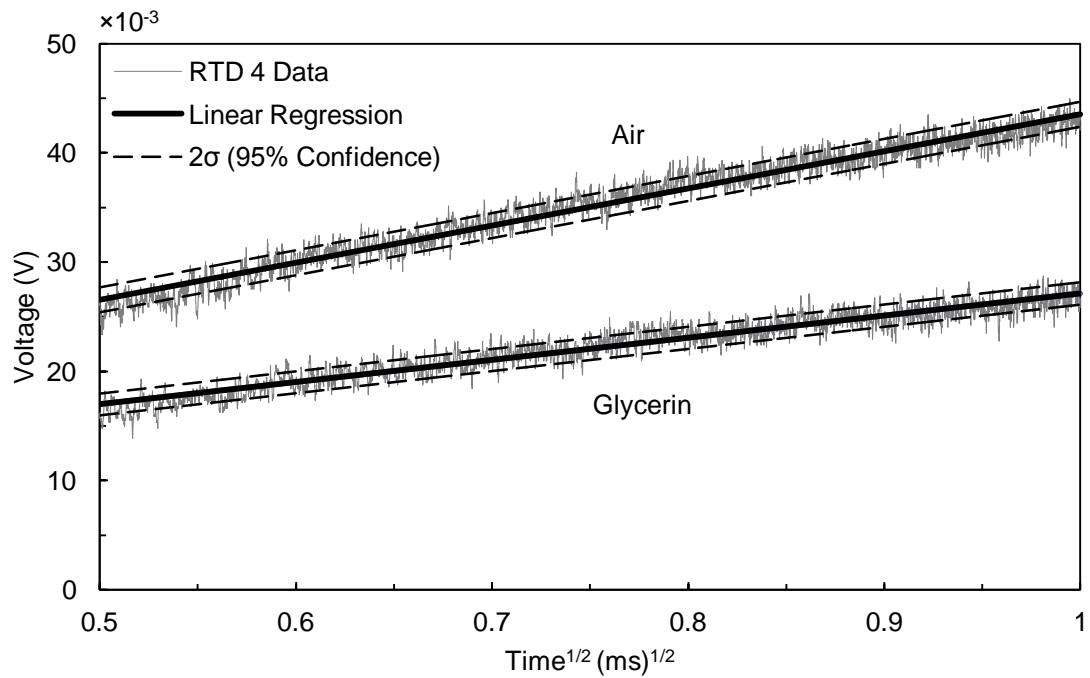
Figure 5.2 Typical dynamic calibration results.

Figure 5.3 Linear relation of voltage and square-root of time.

Figure 5.3 confirms the expected relation by plotting a sample of the superimposed temperature-time data curve against the square root of time and fitting the data with a least-squares linear regression. The data shows minor oscillatory behavior, most likely from an unknown source of impedance, despite efforts to remove all local sources of electromagnetic interference. This behavior reduced the correlation of the regression line with the data, but not to a degree to cause concern. This is evident by the majority of data points still falling between two standard deviations from the linear fit line, including random noise in the output.

Table 5.2 tabulates the pertinent data from the dynamic calibration, including the newly acquired thermal products and linear correlations of each regression. The thermal products of each individual RTD were calculated from the slopes of the linear regressions using equation (3.2) and the known thermal product of the glycerin medium. RTD 1 did not survive this phase, failing due to a prolonged voltage pulse causing electrical burnout.

Table 5.2 Dynamic Calibration Results

RTD	R at 25 °C	β (J/cm^2/K/s$^{0.5}$)	± Total Percent Error	Air Correlation Coefficient	Glycerin Correlation Coefficient
1	47.9	-	-	-	-
2	43.2	0.203	8.85	0.9598	0.9190
3	42.7	0.177	4.93	0.9832	0.9659
4	41.3	0.170	8.59	0.9633	0.9205
5	40.9	0.181	5.76	0.9679	0.9447

<u>5.2 Experimental Results</u>

Test results of the HST low enthalpy calibration tests are presented in this subsection. These include the shock tube data tabulation, the derived results of the array of pressure transducers in the rake, and the calculated surface temperature and heat flux for the single platinum thin film RTD, also in the rake. Data in the test section is differentiated by three test planes, which are measured with respected to the expansion nozzle exit.

5.2.1. Shock Tube

Test conditions at the throat and the expansion nozzle exit into the test section were calculated from a series of equations by initially determining the normal incident shock velocity in the shock tube. This was accomplished using two transducers mounted flush with the interior wall of the shock tube just upstream of the HST throat and then observing their response. Figure 5.4 shows an example of determining the precise time taken for the shock to pass by each sensor.
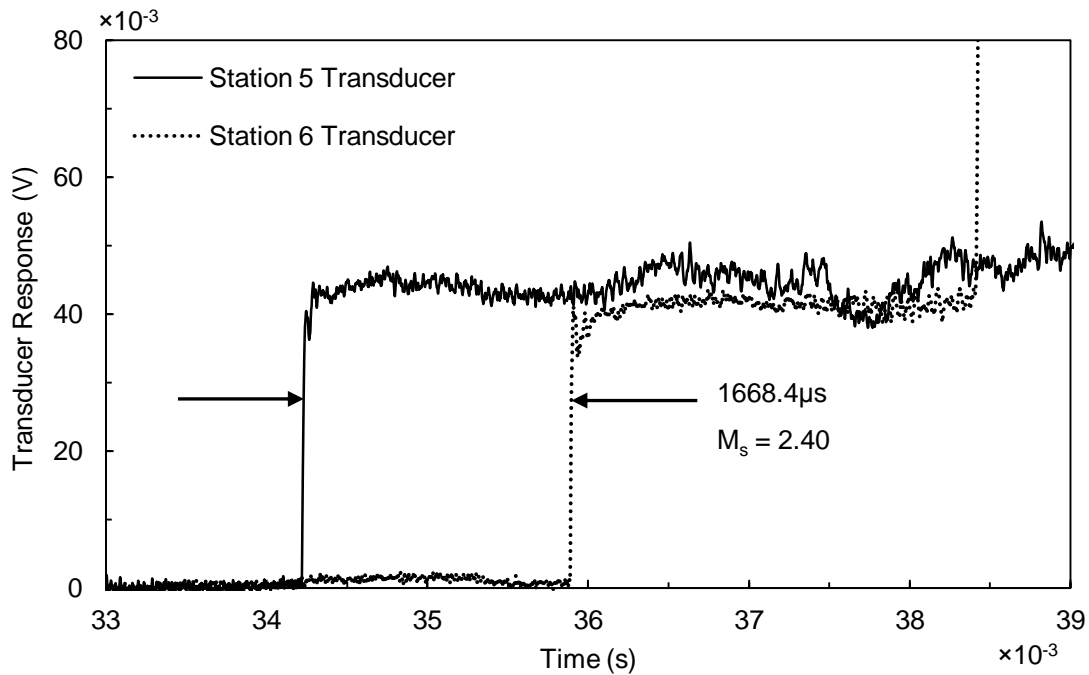

Figure 5.4 Typical shock passage in shock tube.

This measured time was then used to calculate various stagnation and freestream conditions using equation (4.1) through equation (4.5) in conjunction with NASA's online CEA code, CEARUN, used to calculated chemical equilibrium problems, including shock tubes with reflected incident shocks, as is the case in the HST. Results are tabulated in Table 5.3 and are distinguished by their test number and the location of the sensor plane in the test section.

Table 5.3 Test Conditions

Test	x (cm)	M_∞	P_t (MPa)	ρ_t (kg/m^3)	T_t (K)	H_t (kJ/kg)	P_∞ (Pa)	ρ_∞ (kg/m^3)	T_∞ (K)	Re_∞/x (m^{-1})
1	11.783	9.45	2.60	9.99	907.6	639.01	70.55	0.0048	50.8	1.98E+06
2	31.468	9.43	2.74	10.33	923.9	657.27	74.67	0.0050	52.0	2.01E+06
3	51.153	9.42	2.72	10.20	929.6	663.73	74.41	0.0049	52.6	1.96E+06

5.2.2. Transducer Response

Transducer responses from the nine Pitot probes spanning the test section had to be conjointly considered when deciding the useful test time data for each run. Additional consideration had to be given whether a sensor appeared to be within the test section wall boundary layer or not, which effectively reduced the test time. Figure 5.5 shows a typical normalized transducer response for all nine concurrent sensor readings after filtering extraneous noise.
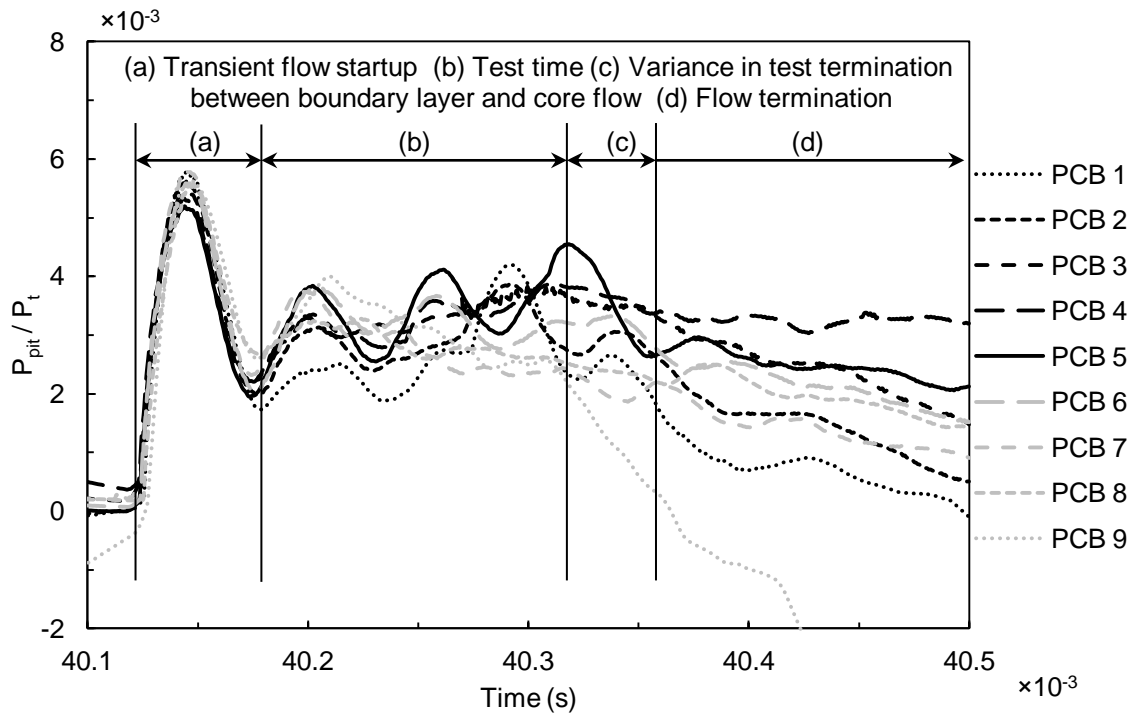
Figure 5.5 Typical Pitot signal pressure-time history in HST test section.

After discerning the useful test time in the core flow and boundary layer regions, the data was then averaged. This can be further refined by removing outlying data from the selected region. Two standard deviations from the mean value have been used in all cases. The three plots in Figure 5.6 show the average measured normalized pressure ratios for each test plane.
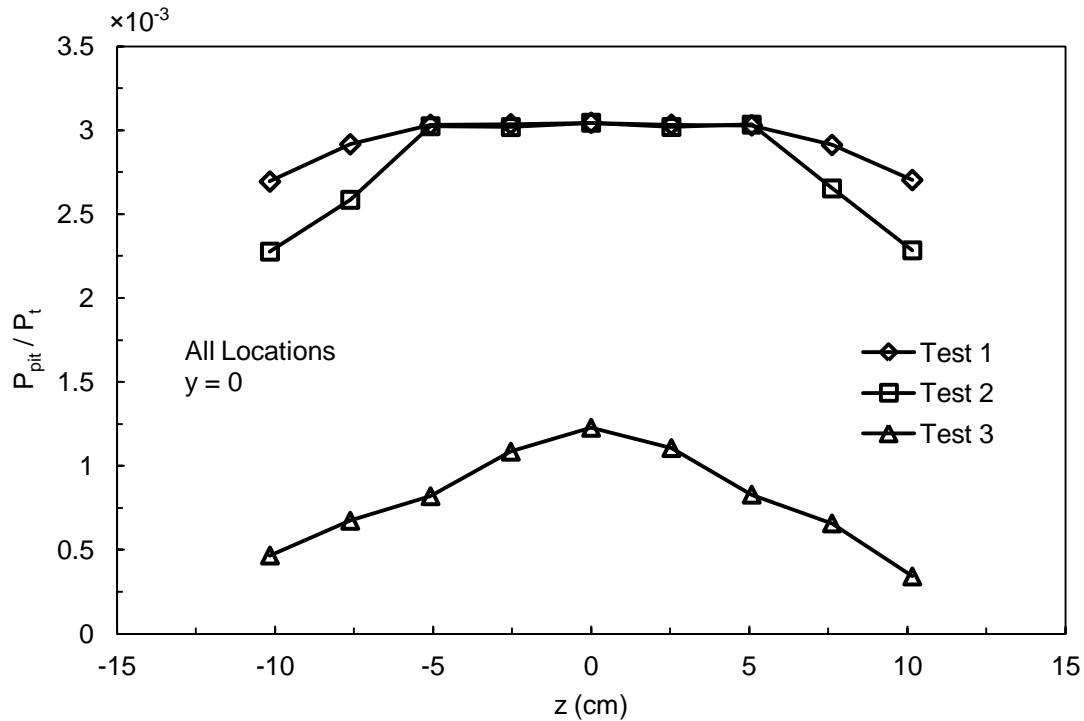
Figure 5.6 Average measured Pitot pressure distributions.

Figure 5.7 shows a sectioned top view of the test section with local Mach numbers at each transducer location, calculated using equation (4.6.) The core flow is traced using a variety of data. The core due to the boundary layer from the expansion nozzle and test section constant area entry is approximated by the results from Test 1 and 2. An oblique shock angle was calculated from the expansion exit using the Taylor-Maccoll method for calculating shocks in conical flow using spherical coordinates [3]. This was accomplished in an expedient manner using previously developed codes following this method [14]. As this test program was

operated under presumed minimum operating conditions for any future experiments, the shock angle would be equal to or less than those observed in this circumstance. This assumption is also dependent on the use of the same Mach 10 nozzle. In addition to the oblique shock, a series of conical expansion waves are formed by the 90° turn at the end of the constant area inlet to the test section. The interaction of these expansion waves with the oblique shock or reflection off of the side walls or diffuser entrance are a possible sources of the flow degradation experienced at the Test 3 plane, as seen on the right side of Figure 5.7.
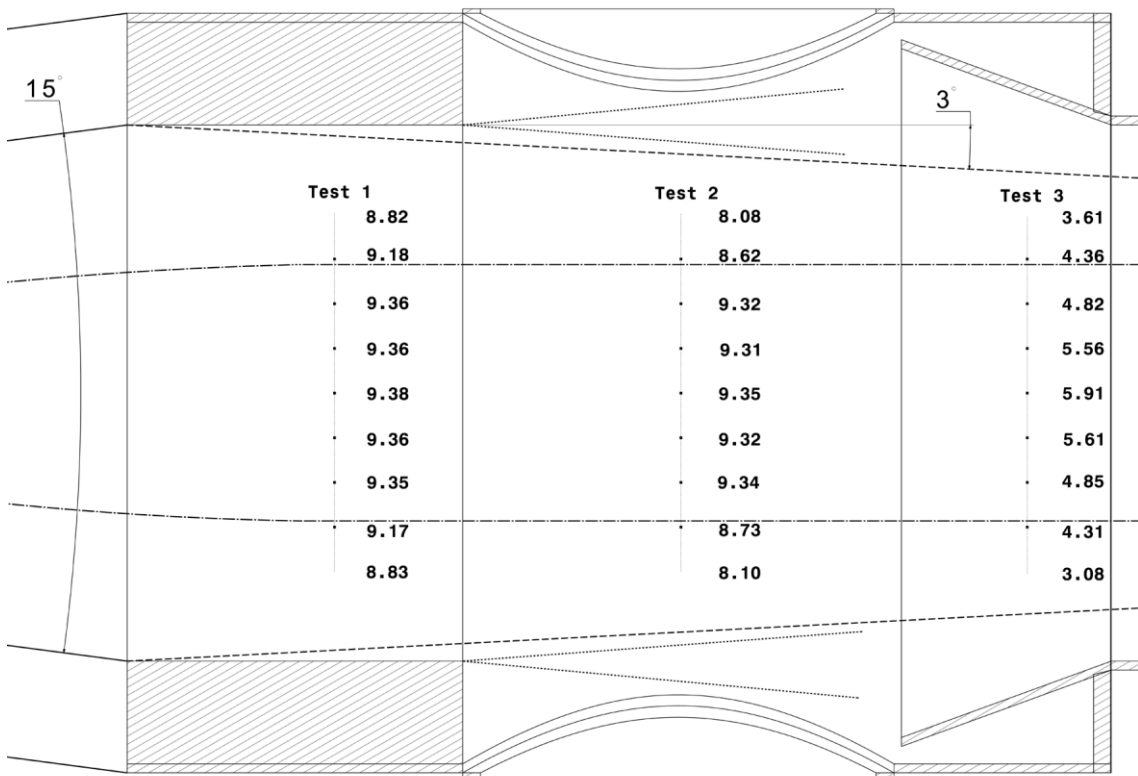
Figure 5.7 Top view of calculated local Mach distributions in test section
with approximate core flow trace.

Figure 5.8 shows the pressure traces at the Test 3 plane, where minimal or no test flow time was experienced. This is apparent from the transition of the signal from the transient startup directly to strong oscillations caused by the driver gas behind the initial shock. Due to this, pressure results from the Test 3 plane are estimated from the termination of the transient startup period for each individual signal, which varies with their positioning relative to the boundary layer.
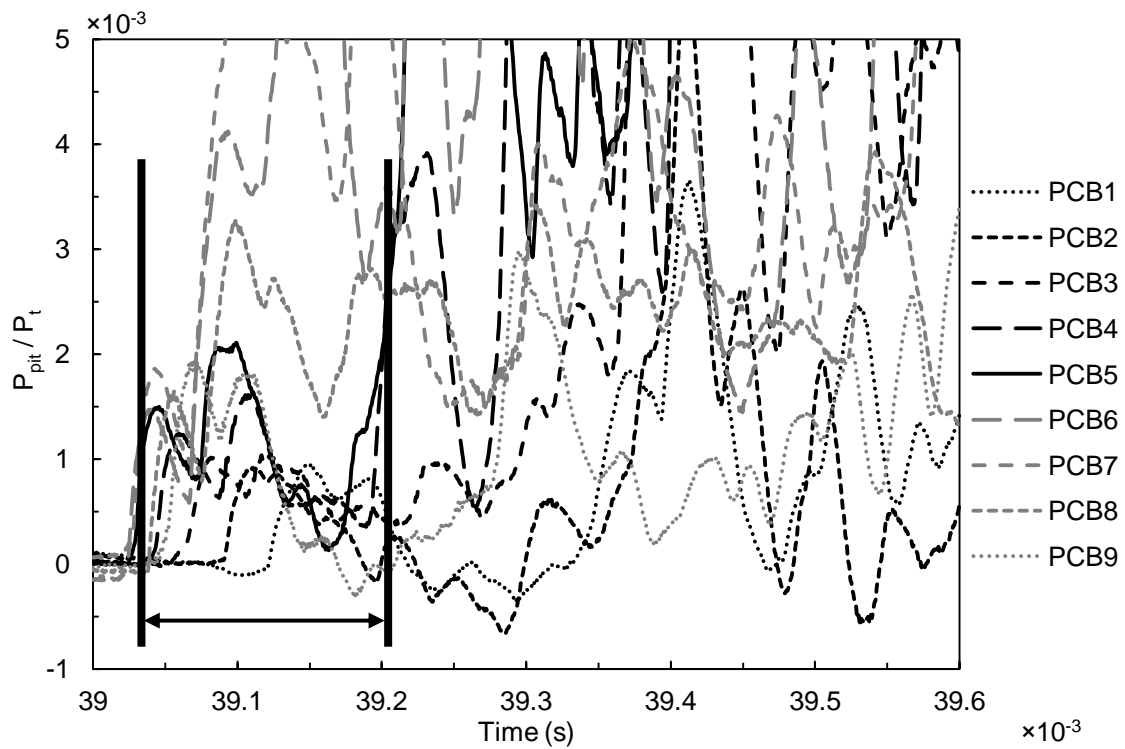
Figure 5.8 Test 3 estimated from end of varying transient startup.

5.2.3. RTD Response

The voltage output for the single RTD lying near the axial centerline of the tunnel for each test was processed to determine the stagnation point temperature rise as well as heat flux under constant and non-constant assumptions.

5.2.3.1 Heat-Flux Determined Via Constant Heat-Flux Case

Voltage responses from the RTD for each test were plotted against the square root of time and fit with a least-squares linear regression to determine the slope need to calculate heat flux using a constant heat flux rate assumption. The slope was obtained and used in equation (4.10) to determine the heat flux for each probe under these ideal circumstances. Some impedance was experienced in each test case, causing oscillations in the results, as shown in Figures 5.9 through 5.11. As the heat flux is determined using only the slope of the regression line, this problem can be mitigated through careful data processing. Also as shown in the same figure, the selected range of data just after a transient startup period fits a linear approximation with an adequate correlation and the majority of points falling between two standard deviations from the regression.
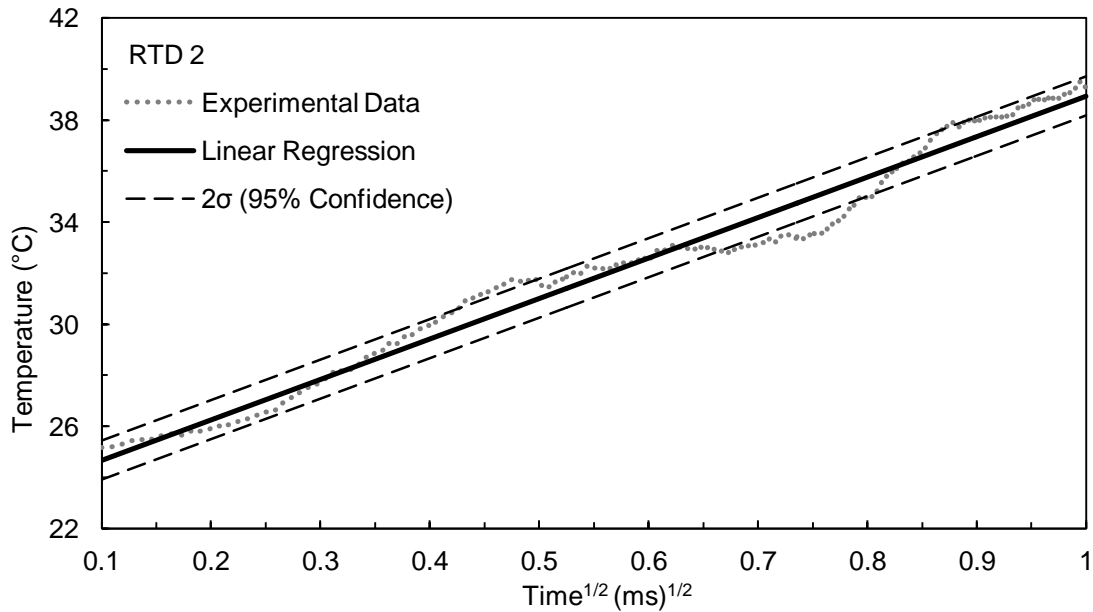
Figure 5.9 Transformed temperature response of RTD 2.
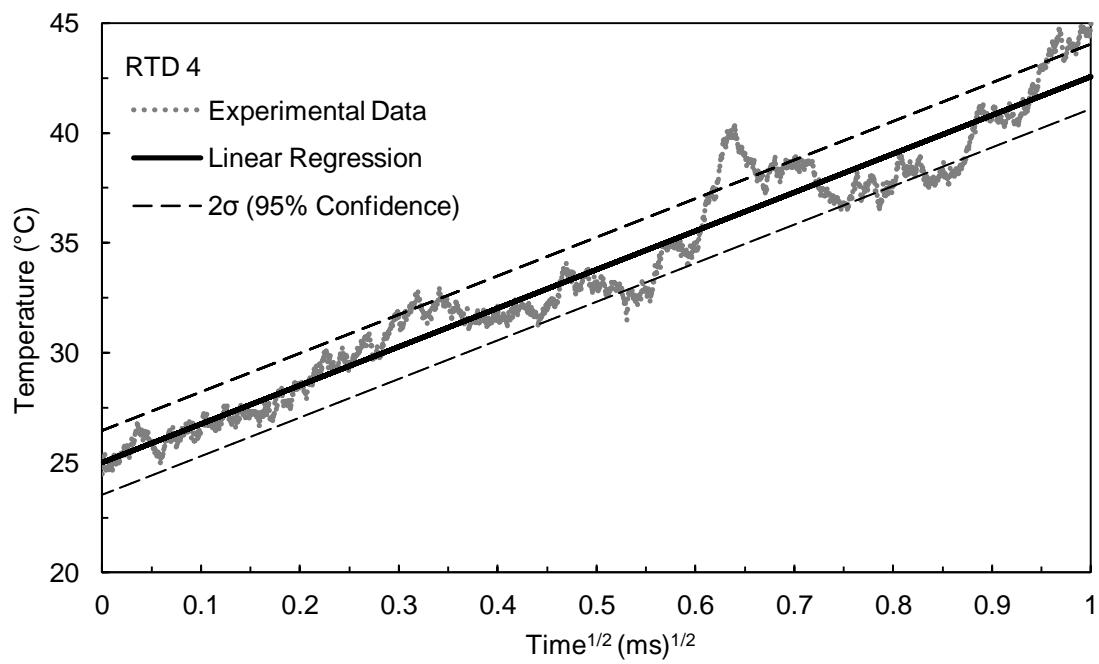
Figure 5.10 Transformed temperature response of RTD 4.
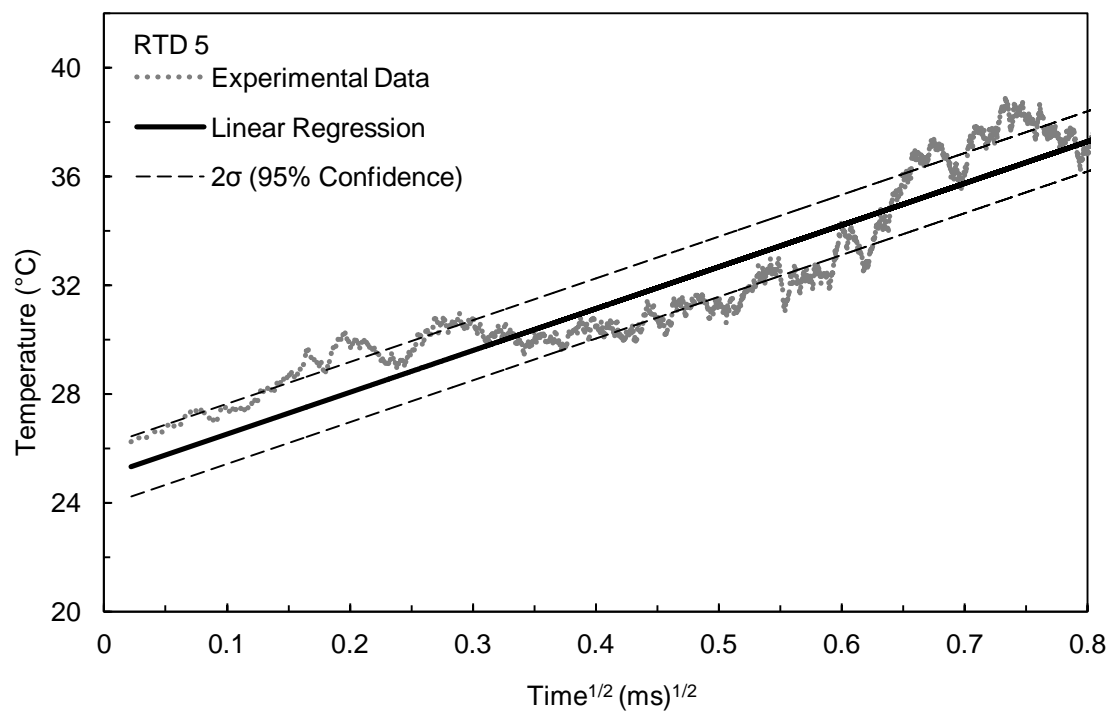
Figure 5.11 Transformed temperature response of RTD 5.

5.2.3.2 Heat-Flux Determined Via Cook-Felderman Algorithm

Using the parabolic fit of the response, the data can processed numerically via the Cook-Felderman algorithm to find the heat flux using a non-constant heat flux assumption. This time was limited to the first millisecond of data for the Tests 1 and 2 to provide a standard by which to compare the results between each test plane. Less than one millisecond of useful test time was present in the response for Test 3 at the back of the test section, most likely due to degradation of the core flow by the intersecting shocks and expansion waves produced upstream in the test section. Figures 5.12 through 5.14 show the results of the RTD using the first millisecond of data with a parabolic fit, except for RTD 5, which only experienced 0.7 ms of useful data..
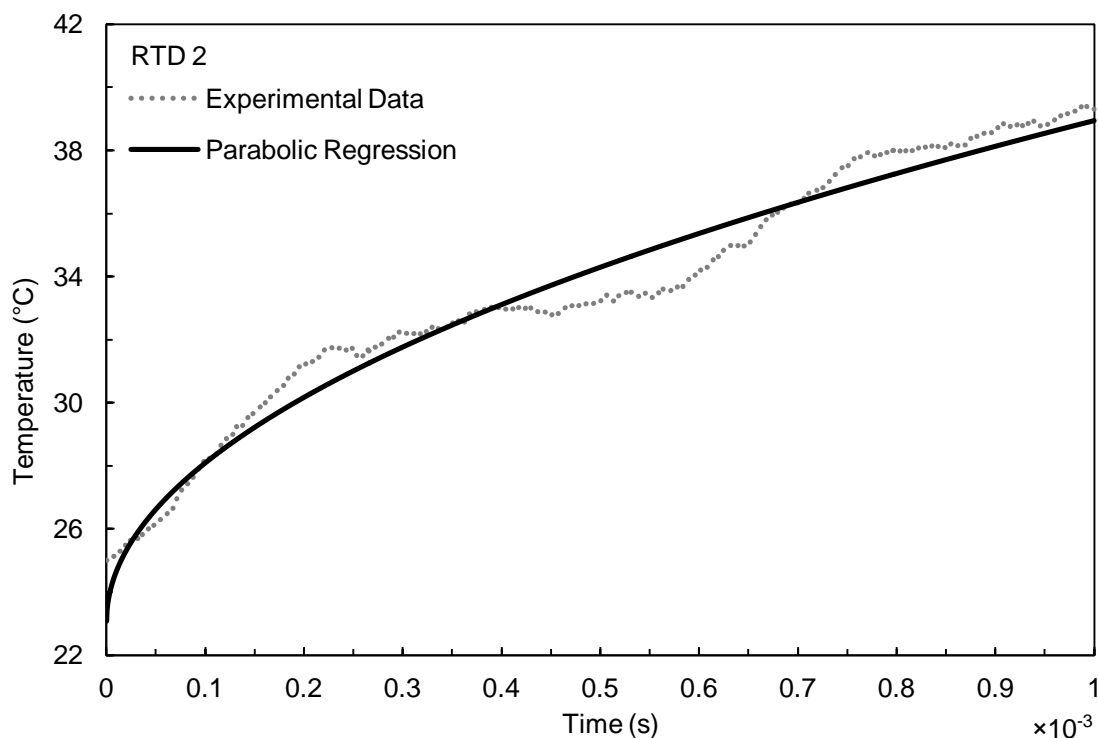
Figure 5.12 Temperature response of RTD 2 with transformed regression.
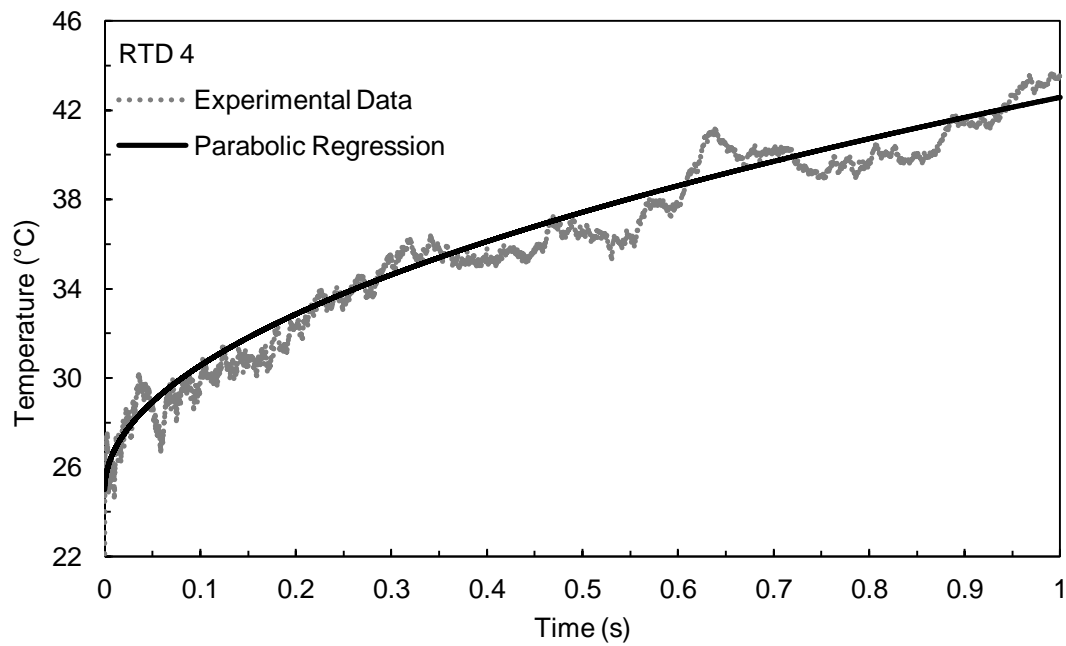
Figure 5.13 Temperature response of RTD 4 with transformed regression.
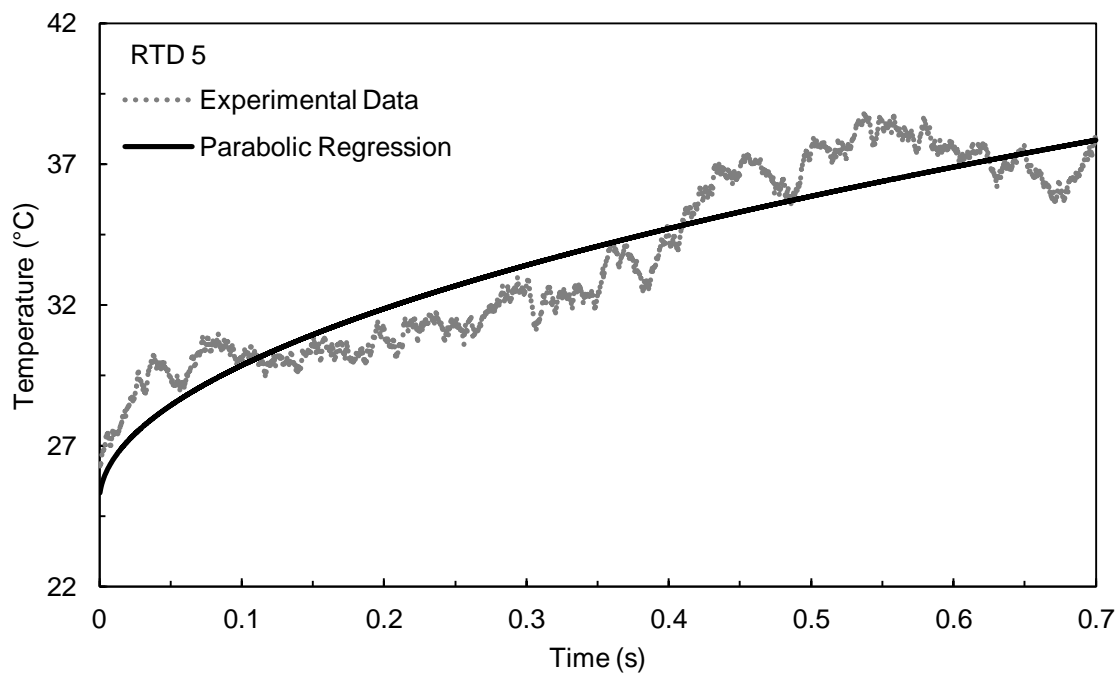
Figure 5.14 Temperature response of RTD 5 with transformed regression.

Equations (4.7a) and (4.7b) can be used with the sensitivities determined during the static calibration to find a conversion factor to convert the voltage response to surface temperatures. Results show that the increase in temperature during the test period caused by the passing shock are fairly minor, increasing by 15-20 °C

Heat flux calculations for the assumed constant and non-constant methods are tabulated in Table 5.4, including the RTD number used for each test, the duration of the useful test time used for the Cook-Felderman algorithm, and the estimated error in each reading caused by the accumulation of errors in each calibration and testing process.

RTD 3 was skipped in the testing process due to electrical burnout while setting up the Wheatstone bridge circuit immediately preceding Test 1. Error in calculated heat flux was estimated from the accumulated linearity error of all regression lines used throughout the calibration and testing data reduction processes.

Table 5.4 Calculated Heat Flux Results

Test	RTD	Constant Heat Flux Case (W/cm^2)	Cook-Felderman (W/cm^2) @ [test time]
1	4	17.2 ± 11.2%	9.37 ± 8.6% @ t = 1.0 ms
2	2	17.86 ± 10.4%	10.49 ± 8.9% @ t = 1.0 ms
3	5	12.16 ± 10.6%	7.80 ± 5.9% @ t = 0.7 ms

CHAPTER 6

CONCLUSIONS AND RECOMMENDATIONS

6.1 Conclusions

All primary objectives of the low enthalpy HST characterization have been completed successfully, including the design and construction of an apparatus to house pressure and temperature sensors at three distinct test section planes under approximately the same operating conditions. A variable length rake and sting system was designed to secure a span of nine pressure transducers across the test section at these locations, which determined the pressure and Mach distribution at these planes. From this data and additional shock calculations, the approximate core flow area was traced.

Platinum thin film RTDs were replicated using a previously documented method. These sensors were incorporated into the rake design and concurrently recorded stagnation temperature and heat transfer rates for each test. Results showed that the probe tip surface temperature increased 15-20 K and the calculated heat flux in the core flow was 9.93 ± 0.56 W/cm^2 for the first millisecond of test time.

Due to possible interference at the back of the test section caused by intersecting oblique shocks and expansion waves generated upstream in the test section, results obtained at the Test 3 plane are suspect. Future tests should be conducted even with or forward of the Test 2 plane at the test section midpoint to avoid these flow complications.

6.2 Recommendations

To improve the quality of heat flux measurements and reduce the error, a more automated manufacturing method should be implemented to remove as much human involvement as possible. Nanofabrication is a quickly growing industry that could suit thin film applications such as those employed in this study. This would allow for a large number of nearly identical sensors to be easily replicated and used in great quantities for single tests.

The durability of the thin film sensors must also be addressed. Additional construction steps to add a highly heat conductive but strong coating material over the films would greatly increase their durability.

The sting primary and secondary arms can be reused or modified to accommodate a wide variety of models at any test plane between the Test 1 and Test 3 by simply drilling additional screw holes. This allows for a 39.37 cm (15.5 in.) axial range of flexibility between points near the front and back of the test section. Additionally, a rubber O-ring could potentially be added to the sting interlocking pipe fitting to remove deficiencies in the connection caused by wear from repeated use.
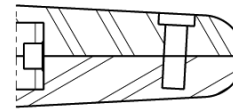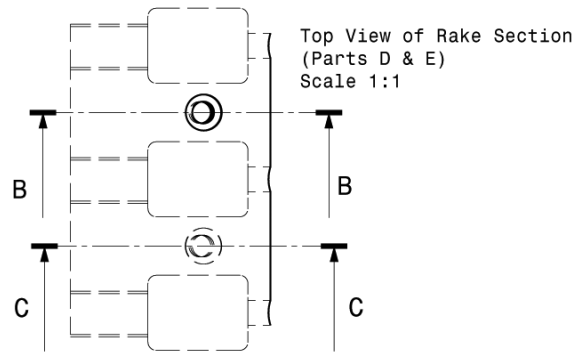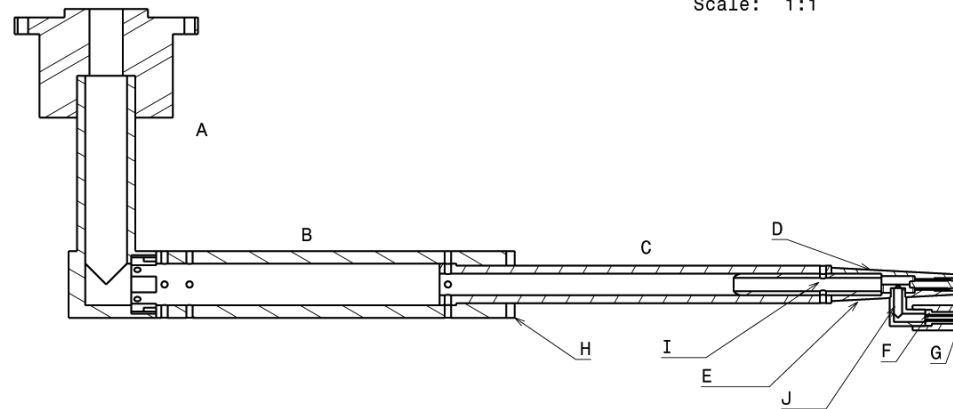
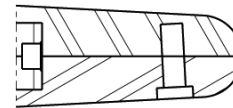APPENDIX A

RAKE & STING ASSEMBLY AND PART DESIGN

A

B

C

D

E

F

G

H

I

J
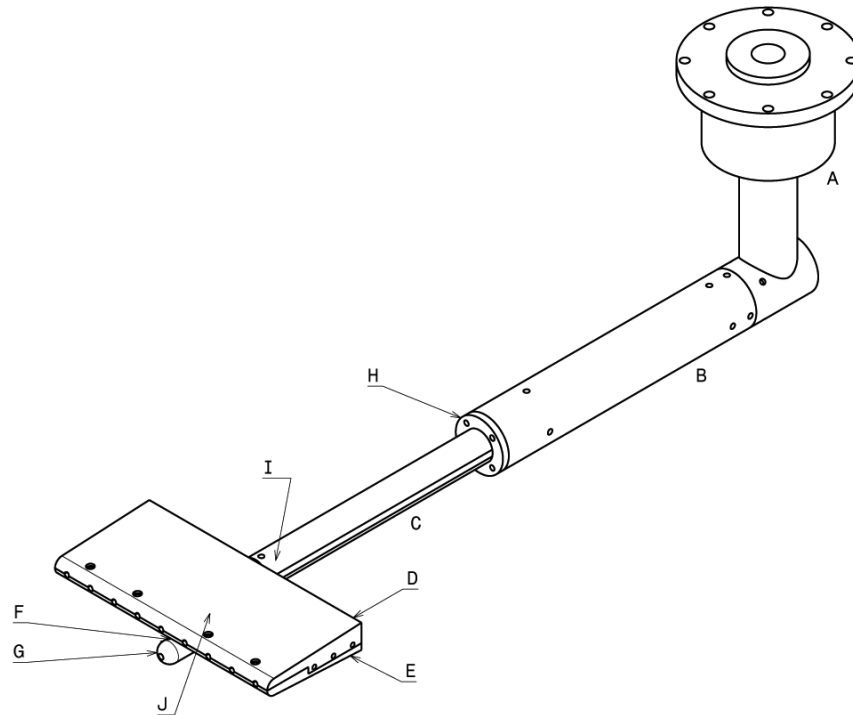
UTA AERODYNAMICS REASEARCH CENTER		
PAGE: ASSEMBLY ISOMETRIC VIEW		
MATERIAL: ALUMINUM		
SCALE: 1:4	DRAWN BY: D.LEAMON	DATE: 29 AUG 2011

A

D

63

f
f

Kx9

i
h   i
h   i   g
G   F   J   E

d

I

d

B

b,c

c   b

H

C

UPPERCASE: Part

lowercase: Connections
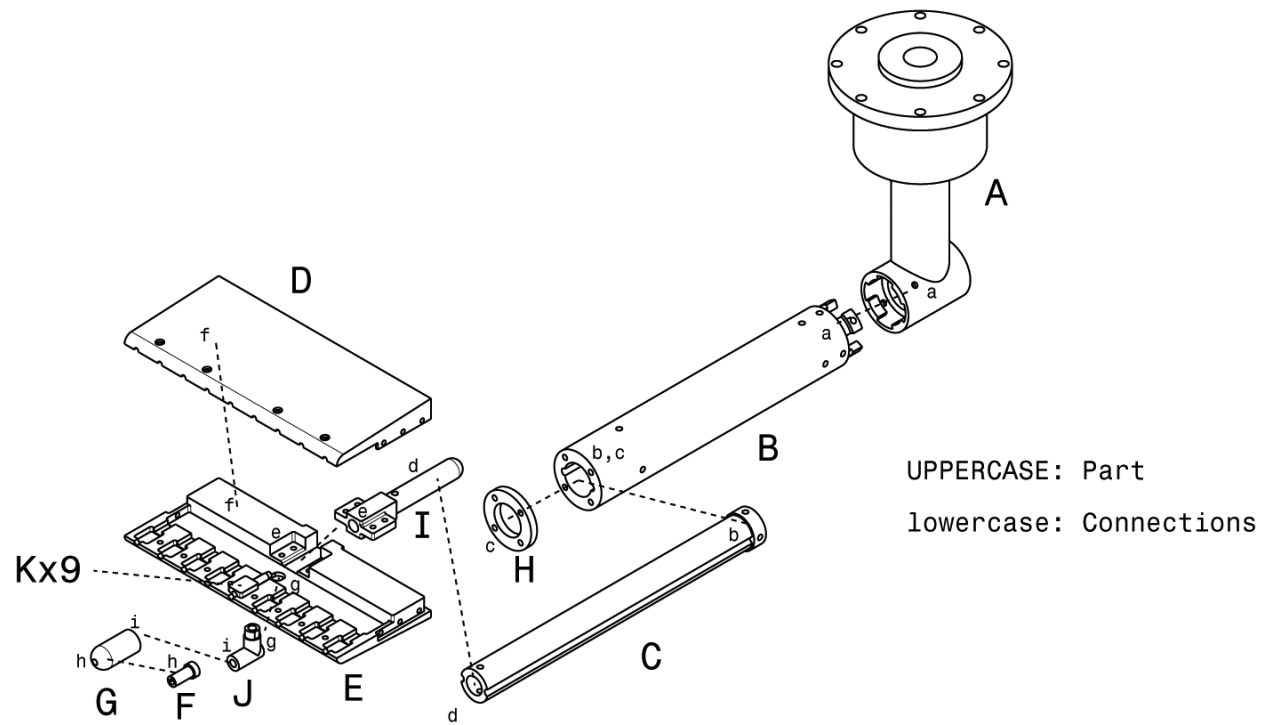
UTA AERODYNAMICS REASEARCH CENTER		
PAGE: ASSEMBLY EXPLODED ISOMETRIC		
MATERIAL: ALUMINUM		
SCALE: 1:4	DRAWN BY: D.LEAMON	DATE: 29 AUG 2011

Top View of Rake Section
(Parts D & E)
Scale 1:1

B

B

C

C

See Parts D & E

Section View B-B
Scale: 1:1

Section View C-C
Scale: 1:1

A

B

C

D

H

I

E

J

F

G

UTA AERODYNAMICS REASEARCH CENTER		
PAGE: ASSEMBLY SECTIONED VIEW		
MATERIAL: ALUMINUM		
SCALE: 1:4	DRAWN BY: D.LEAMON	DATE: 29 AUG 2011

3.25
2
0.75
0.25

Front View

Top View

∅5.5
∅2.5
∅1
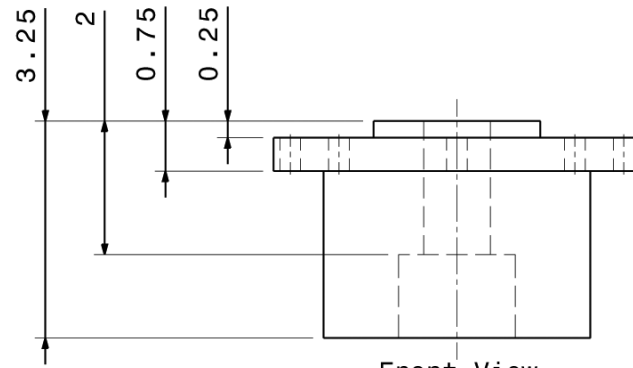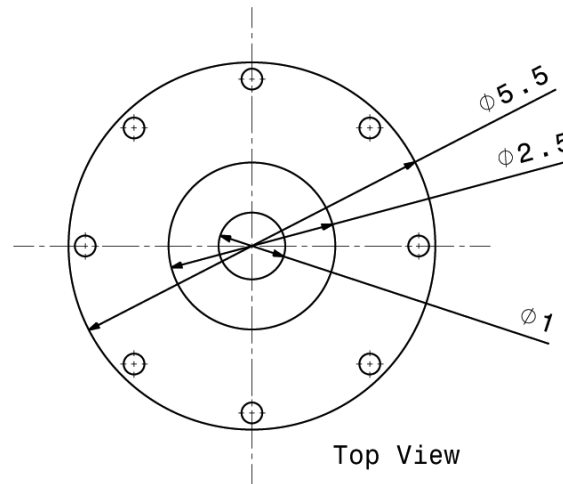
DIMENSIONS IN INCHES

UTA AERODYNAMICS REASEARCH CENTER		
PAGE: 1 OF A1		
MATERIAL: ALUMINUM		
SCALE: 1:2	DRAWN BY: D.LEAMON	DATE: 28 JUNE 2011
TOLERANCES:	.X	0.01
	.XX	0.001

45°

2.5

⌀0.312

⌀4

⌀1.75

Bottom View

Isometric View
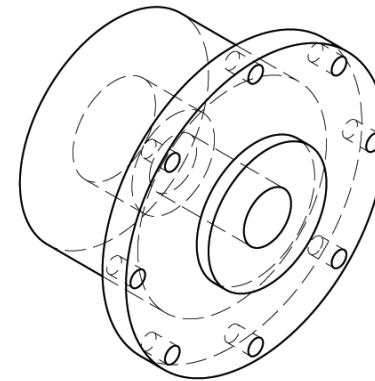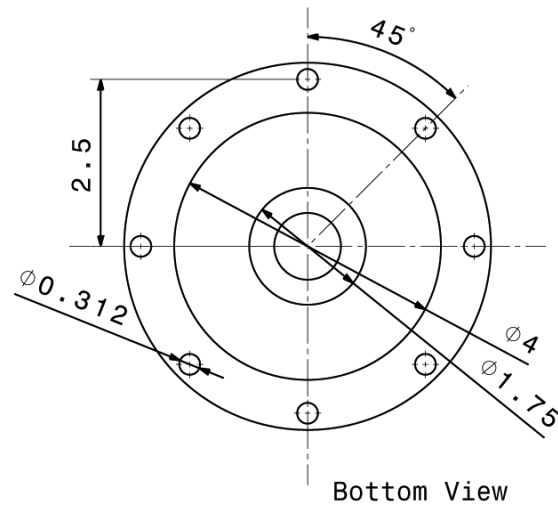
DIMENSIONS IN INCHES

UTA AERODYNAMICS REASEARCH CENTER		
PAGE: 2 OF A1		
MATERIAL: ALUMINUM		
SCALE: 1:2	DRAWN BY: D.LEAMON	DATE: 28 JUNE 2011
TOLERANCES:	.X	0.01
	.XX	0.001
	.XXX	0.0005

Top View

2.625 1.875 1.125

Section View A-A
Scale: 1:1

A_3

0.75
0.5625
0.375

A_2

A_1

6.25

A

A_4   A   Front View

Right View

⌀1.75
⌀1.25
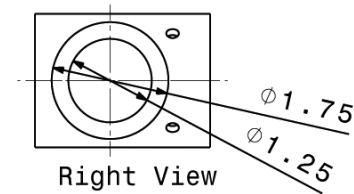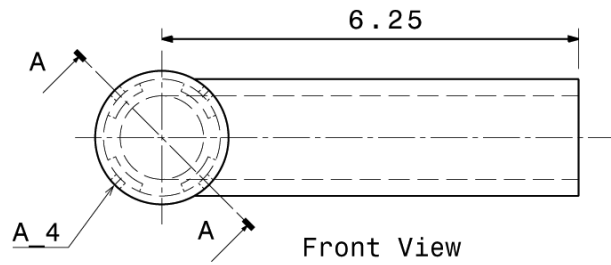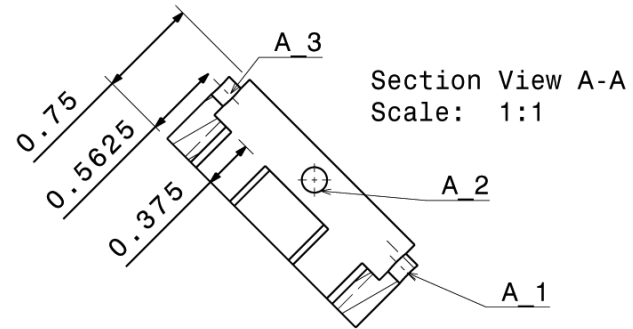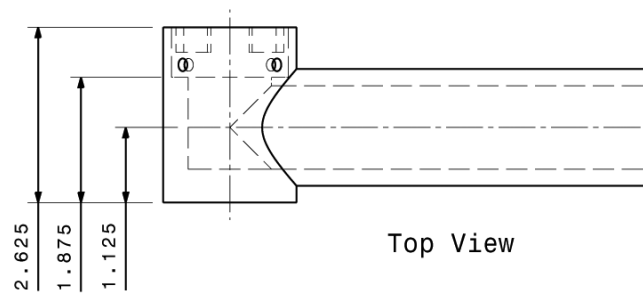
THREAD TABLE	
A_1-A_4	10-32 UNC-2B THRU

UTA AERODYNAMICS REASEARCH CENTER		
PAGE: 1 OF A2		
MATERIAL: ALUMINUM		
SCALE: 1:2	DRAWN BY: D.LEAMON	DATE: 25 AUG 2011
TOLERANCES:	.X	0.01
	.XX	0.001
	.XXX	0.001

DIMENSIONS IN INCHES
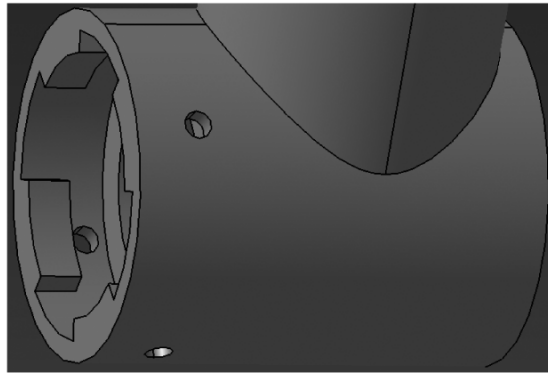
Detail A2
Isometric Image
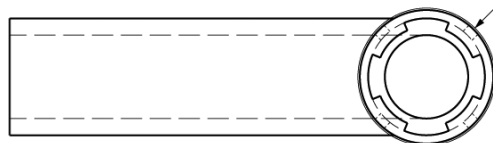
Rear View
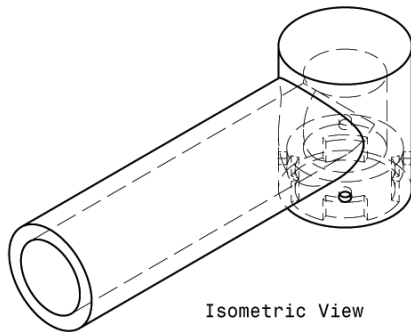
Isometric View

See Detail A2

22.5°

45°

67.5°

90°

B

A_3

A_2

⌀1.5

⌀1.25

⌀1.75

⌀2

A_2

A_1

A_4

B

Detail A2
Scale: 2:1

A_2

A_1

A_1

A_4
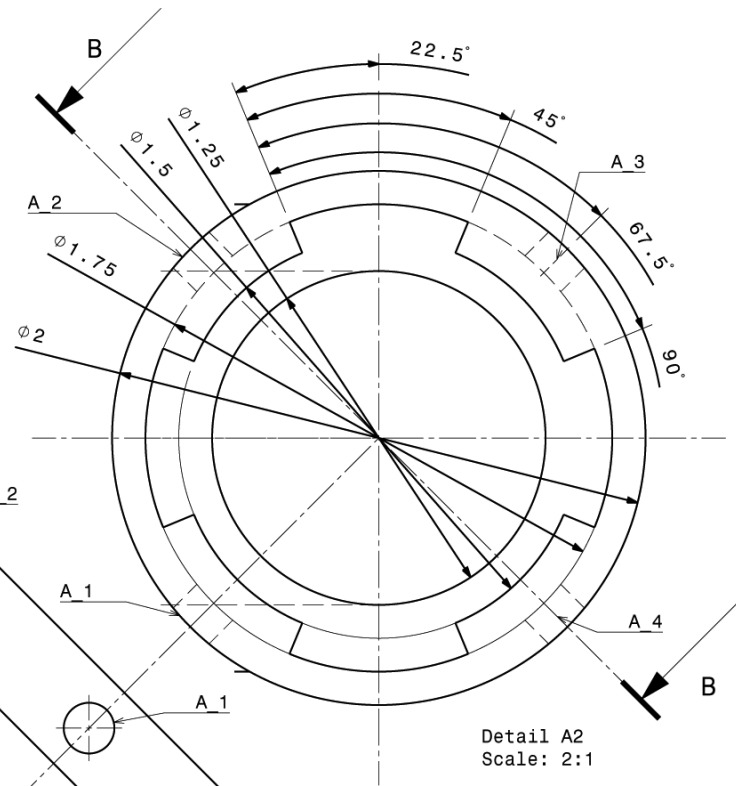
Section View B-B
Scale: 2:1

THREAD TABLE	
A_1-A_4	10-32 UNC-2B THRU

UTA AERODYNAMICS REASEARCH CENTER		
PAGE: 2 OF A2		
MATERIAL: ALUMINUM		
SCALE: 1:2	DRAWN BY: D.LEAMON	DATE: 25 AUG 2011
TOLERANCES:	.X	0.01
	.XX	0.001
	.XXX	0.001

DIMENSIONS IN INCHES

A1

A2

Side View

Isometric View

Bottom View
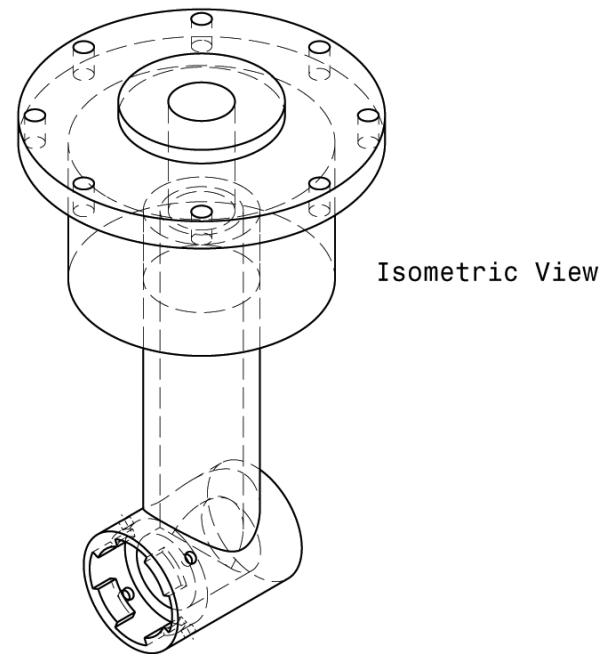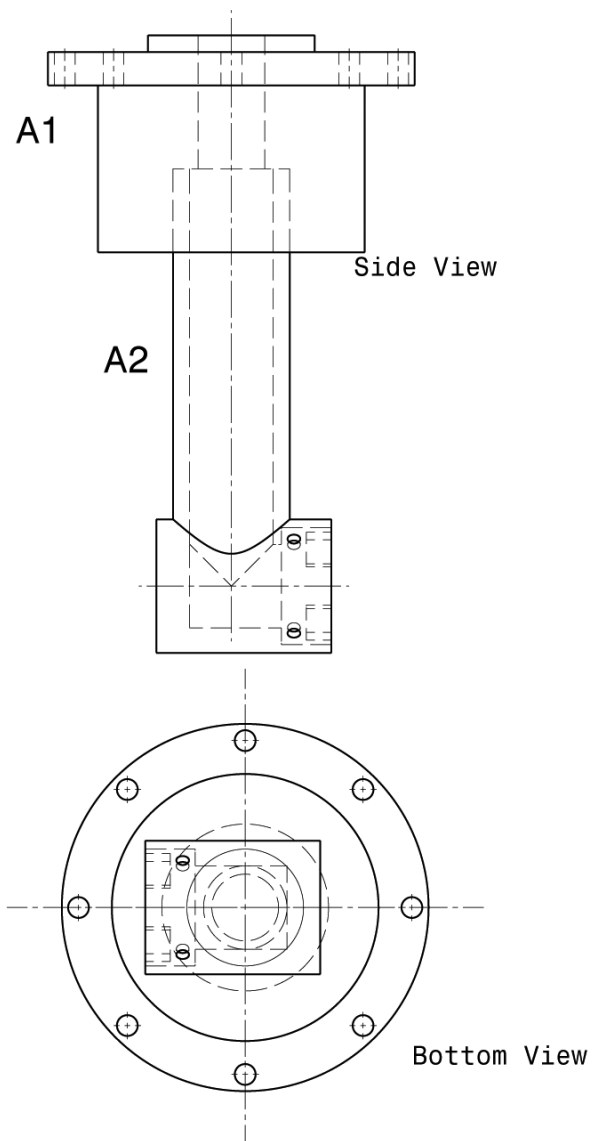
UTA AERODYNAMICS REASEARCH CENTER		
PAGE: 1 OF A (ASSEMBLED)		
MATERIAL: ALUMINUM		
SCALE: 1:2	DRAWN BY: D.LEAMON	DATE: 28 JUNE 2011

Top View

22.5° 45° 67.5°
90°
Ø1.5
Ø1.75
Ø1.25

Front View
Scale 1:3

13B-16B
9B-12B
5B-8B

1B-4B

B_20
B_17
45°
R0.125
Ø2
B_19
B_18
Ø1.125
Bottom View

0.75
0.5625
0.375

Auxiliary View
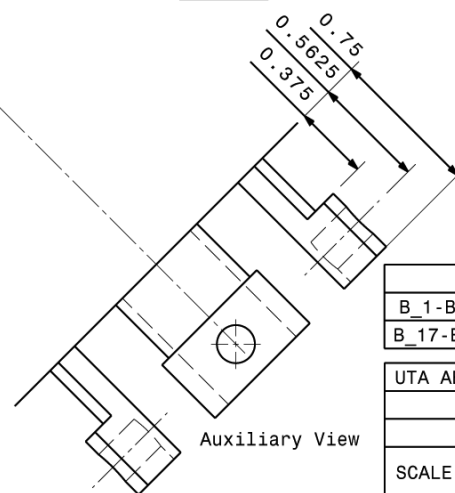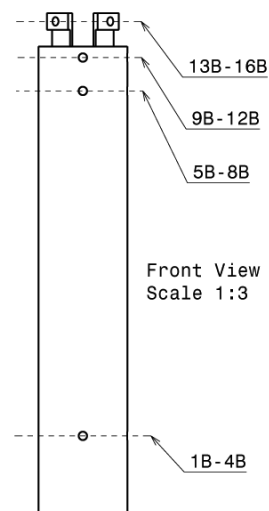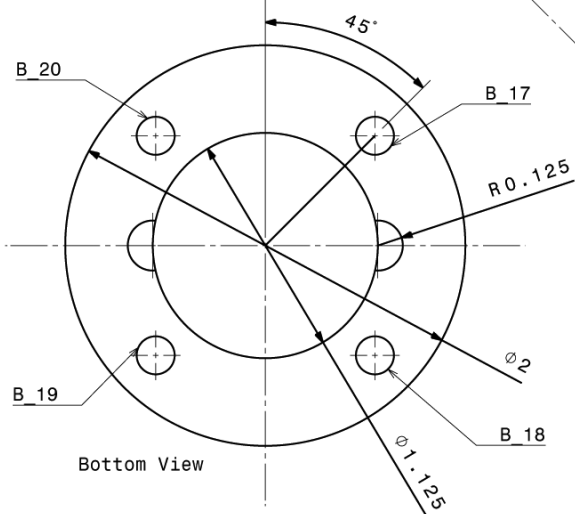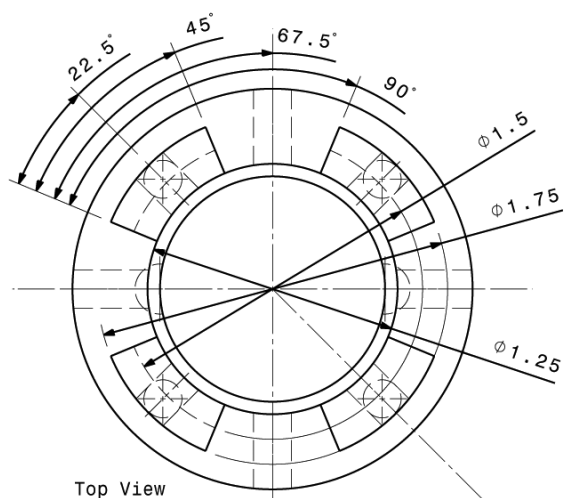
DIMENSIONS IN INCHES

THREAD TABLE	
B_1-B_16	10-32 UNC-2B THRU
B_17-B_20	10-32 UNC-2B X0.85

UTA AERODYNAMICS REASEARCH CENTER		
PAGE: 1 OF B		
MATERIAL: ALUMINUM		
SCALE: 3:2	DRAWN BY: D.LEAMON	DATE: 25 AUG 2011
TOLERANCES:	.X	0.01
	.XX	0.001
	.XXX	0.001

B

B_13-B_16

B_9-B_12

B_5-B_8

11.25

10.5

10.25

9.5

B_1-B_4

1.75

1.5

B_17
B_18

B_19
B_20

B

Front View

1.375

1.5

Section View B-B

Isometric View
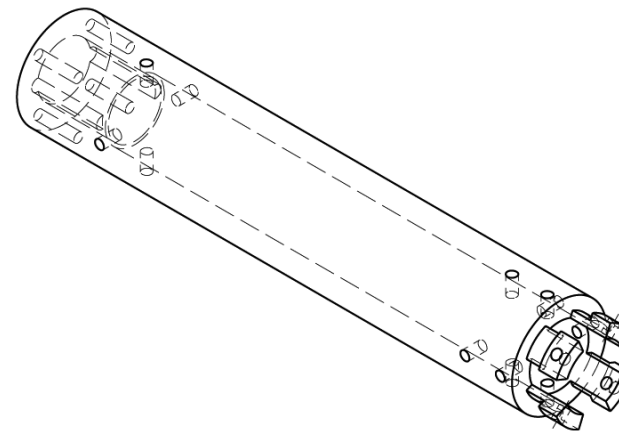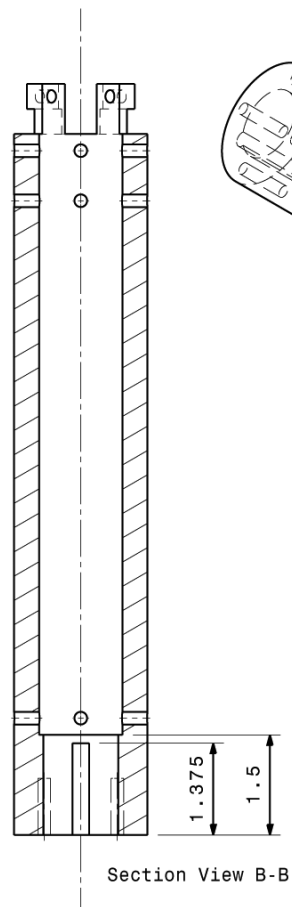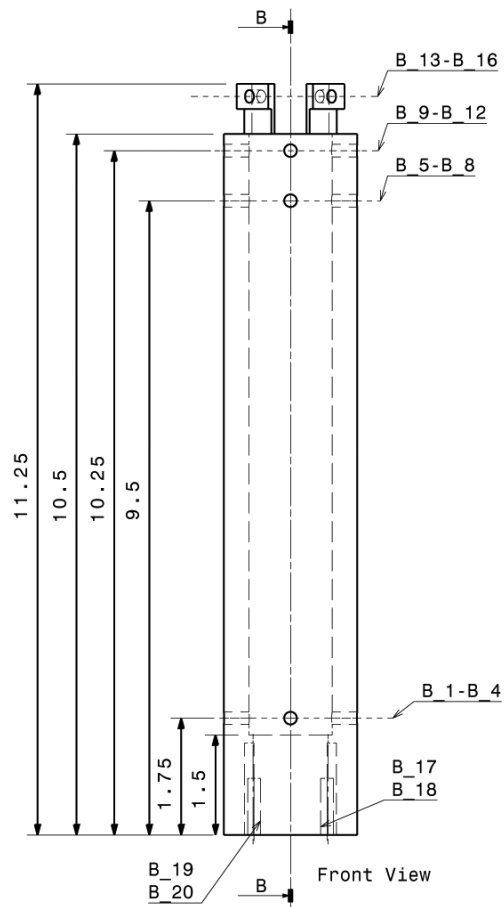
THREAD TABLE	
B_1-B_16	10-32 UNC-2B THRU
B_17-B_20	10-32 UNC-2B X0.85

UTA AERODYNAMICS REASEARCH CENTER		
PAGE: 2 OF B		
MATERIAL: ALUMINUM		
SCALE: 1:2	DRAWN BY: D.LEAMON	DATE: 25 AUG 2011
TOLERANCES:	.X	0.01
	.XX	0.001
	.XXX	0.001

DIMENSIONS IN INCHES

C_4

A

C_3

C_5

C_1

A

Front View

C_3

C_6

C_4

11.25

11.5

11.75

C_1

0.25

C_2

Section View A-A

Φ0.65

Φ1.125

Φ1.25

R0.125

Bottom View
Scale 2:1
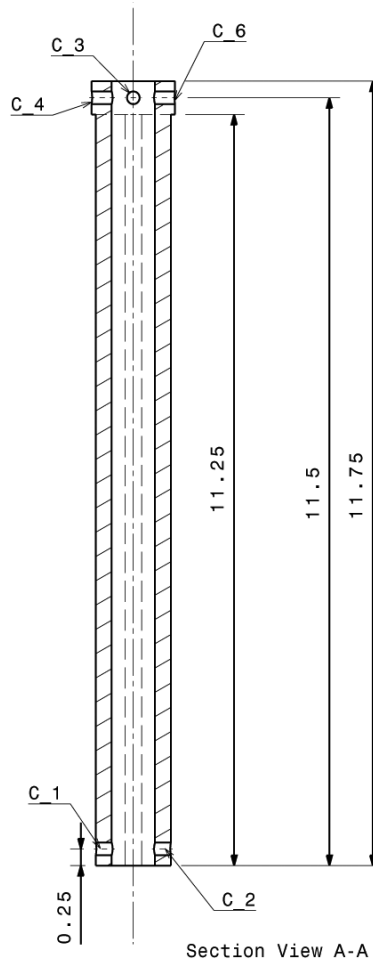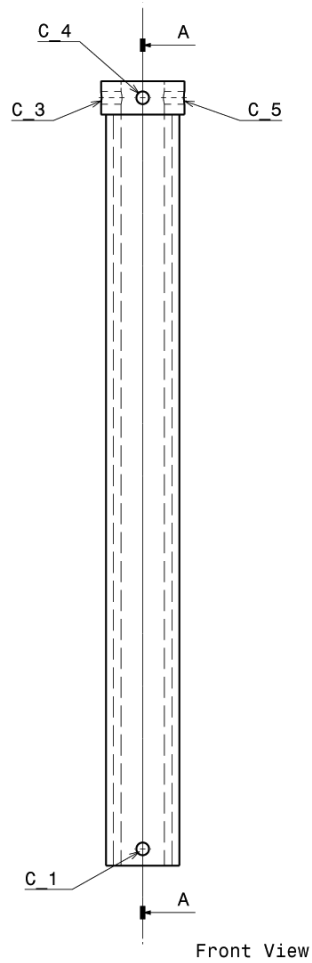
DIMENSIONS IN INCHES
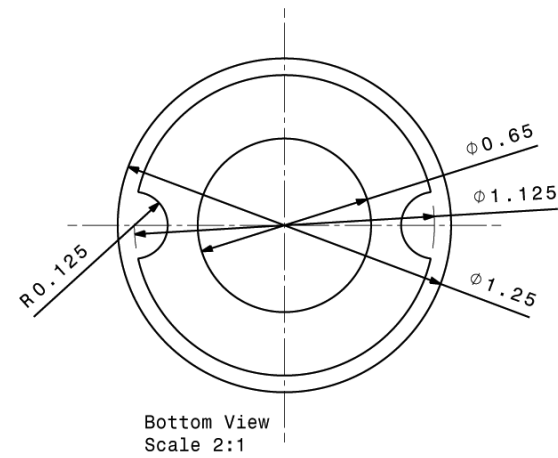
THREAD TABLE	
C_1-C_6	10-32 UNC-2B THRU

UTA AERODYNAMICS REASEARCH CENTER			
PAGE: 1 OF C			
MATERIAL: ALUMINUM			
SCALE: 1:2	DRAWN BY: D.LEAMON	DATE: 24 AUG 2011	
TOLERANCES:		.X	0.01
		.XX	0.001
		.XXX	0.001

C_4

C_3   C_5

Isometric View

C_6

C_2

C_5

C_3

C_1

C_4   Top View
                       Scale: 2:1

C_1

Front View

THREAD TABLE	
C_1-C_6	10-32 UNC-2B THRU

UTA AERODYNAMICS REASEARCH CENTER		
PAGE: 2 OF C		
MATERIAL: ALUMINUM		
SCALE: 1:2	DRAWN BY: D.LEAMON	DATE: 24 AUG 2011

Bottom View

See Detail D1

0.1625
0.1875

9
8.875
8.75
0.25
0.125

Detail D1
Scale: 4:1

R0.075

3°

D_3
D_2
D_4 D_5 D_6
1.5
D_7 D_8 D_9 D_10
D_11

D_10
D_11
D_12

D_1 D_13 D_14 D_15 D_16 D_12
D_17 D_18 D_19 D_20

R0.306

Left View

2.5
2.25
1.5
0.125

0.2188
0.3563
0.6813
0.7813

Rear View

See Detail D2

D_4 D_5 D_6 D_7 D_8 D_9

0.75
0.625

0.5
0.25

Top View

0.1625
0.075

Detail D2
Scale: 4:3

Fillets and Rounds: 1/16"

DIMENSIONS IN INCHES

THREAD TABLE	
D_1-D_16	8-32 UNC-2B THRU
D_17-D_20	8-32 UNC-2B (HELICOIL) X0.243

UTA AERODYNAMICS REASEARCH CENTER			
PAGE: 1 OF D			
MATERIAL: ALUMINUM			
SCALE: 2:3	DRAWN BY: D.LEAMON	DATE: 15 AUG 2011	
TOLERANCES:		.X	0.01
		.XX	0.001
		.XXX	0.001

74

8.175

6.925

5.675

4.5

3.325

2.075

0.825

D_3

D_2

D_4 D_5 D_6 D_7 D_8 D_9 D_10

D_11

D_1 D_13 D_14 D_15 D_16 D_12

D_17 D_18 D_19 D_20

2

1.1875 0.375

1.875

0.5

1.5

Rear View

Isometric View
Scale: 1:3
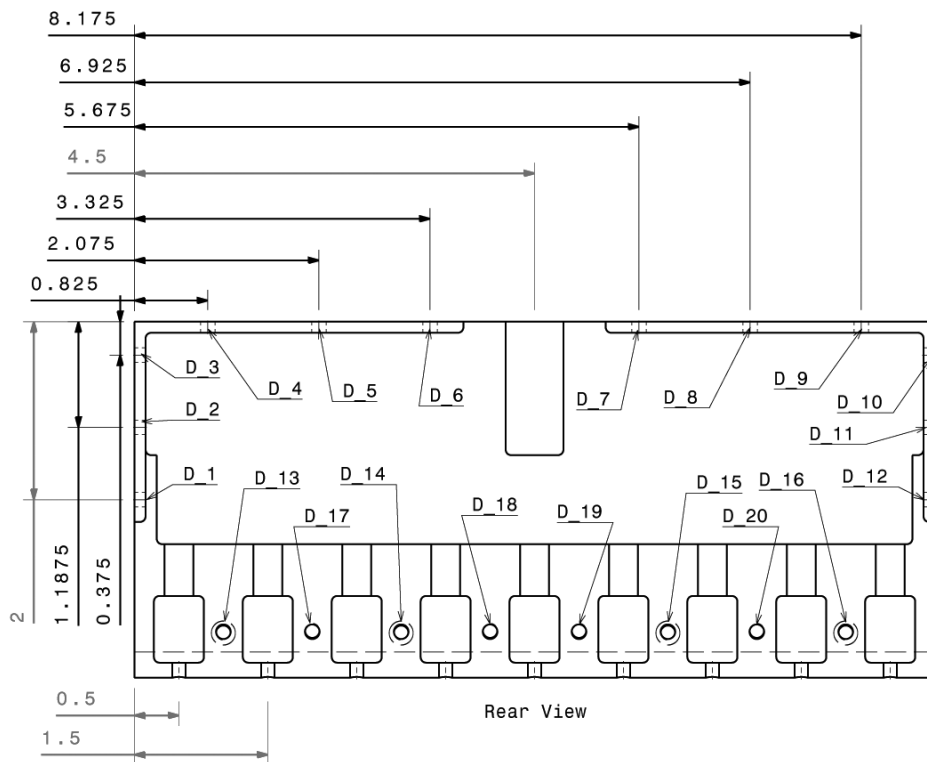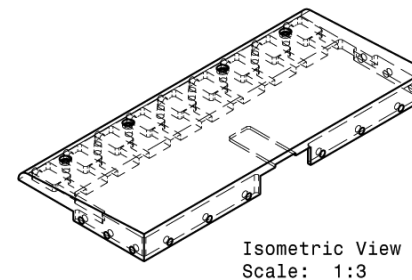
THREAD TABLE	
D_1-D_16	8-32 UNC-2B THRU
D_17-D_20	8-32 UNC-2B (HELICOIL) X0.243

UTA AERODYNAMICS REASEARCH CENTER			
PAGE: 2 OF D			
MATERIAL: ALUMINUM			
SCALE: 2:3	DRAWN BY: D.LEAMON	DATE: 15 AUG 2011	
TOLERANCES:		.X	0.01
		.XX	0.001
		.XXX	0.001

Fillets and Rounds: 1/16"

DIMENSIONS IN INCHES

Section View D-D
Scale: 1:1

D_13-D_16

0.085   D_13-D_16

∅0.27

93°

0.5

Auxiliary View
Scale: 1:1

D_17-D_20

0.5163

87°

Section View E-E
Scale: 1:1

D_3
D_4   D_5   D_6   D_7   D_8   D_9
D_2   D_10
D_11
D_1   D_13   D_14   D_15   D_16   D_12
D_17   D_18   D_19   D_20

Rear View

0.5

1.5

DIMENSIONS IN INCHES

THREAD TABLE	
D_1-D_16	8-32 UNC-2B THRU
D_17-D_20	8-32 UNC-2B (HELICOIL) X0.243

UTA AERODYNAMICS REASEARCH CENTER		
PAGE: 3 OF D		
MATERIAL: ALUMINUM		
SCALE: 2:3	DRAWN BY: D.LEAMON	DATE: 15 AUG 2011
TOLERANCES:	.X	0.01
	.XX	0.001
	.XXX	0.001

Fillets and Rounds: 1/16"

77

Front View

E_3, E_4, E_2, E_5, E_18, E_17, E_1, E_7, E_19, E_6, E_8, E_9, E_20, E_10, E_12, E_21, E_22, E_13, E_14, E_15, E_16, E_23, E_24, E_11

9
8.875
8.75
0.25
0.125
0.825
0.575
0.325
0.8
4
2.5
2.25
1.5
0.125
0.9188
0.1688
0.2188
0.7813

Left View

E_2, E_1, E_12
1.5
0.382
0.25
R0.306

2
1
0.75
0.5

Bottom View

See Detail E1

Detail E1
Scale: 4:1
R0.0938
0.1625
0.1875

Fillets and Rounds: 1/16"

DIMENSIONS IN INCHES
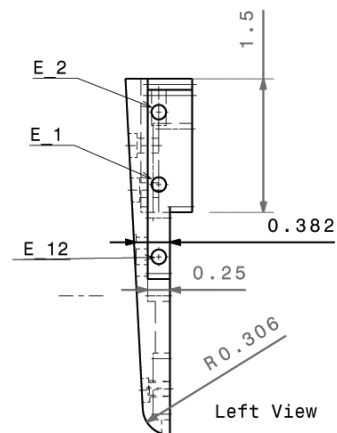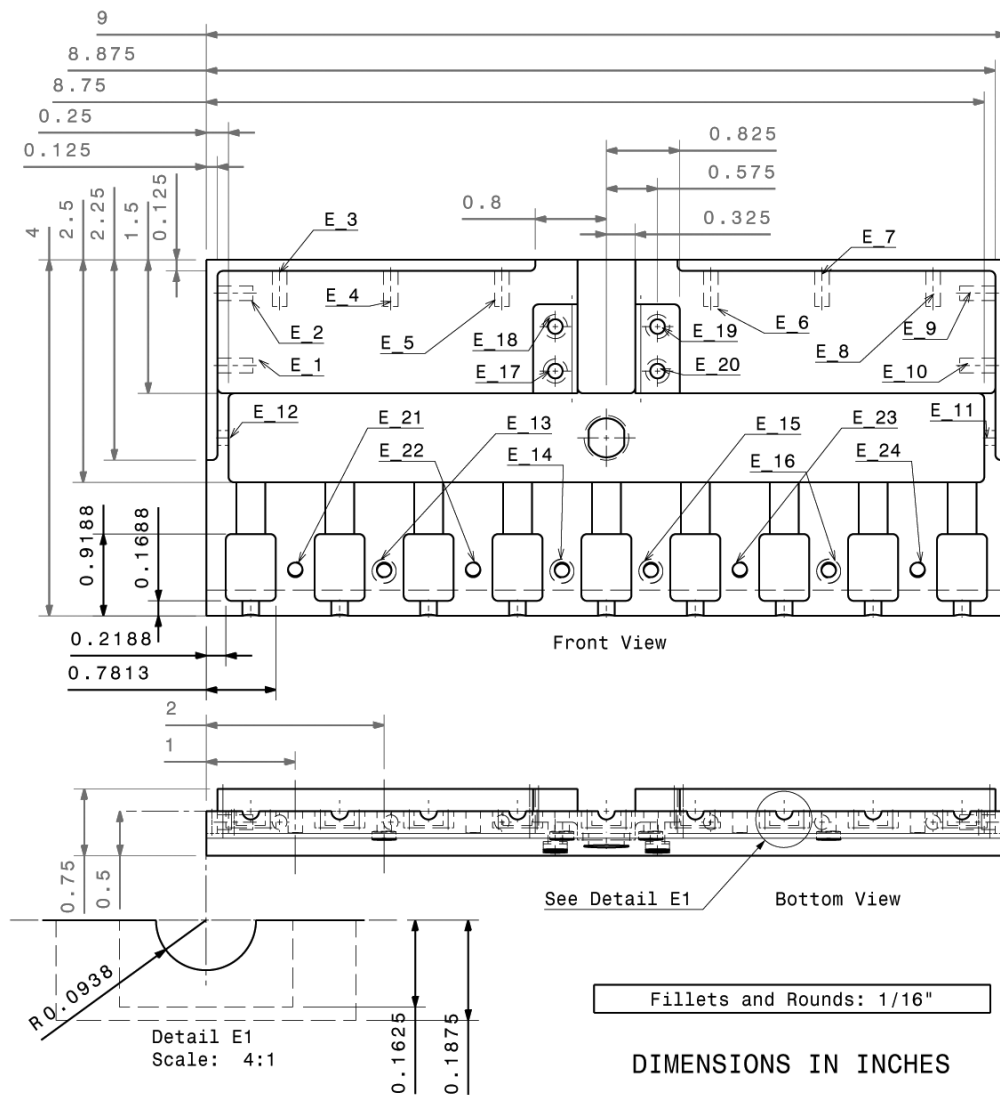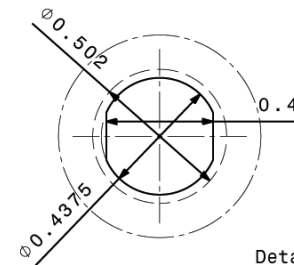
THREAD TABLE	
E_1-E_10	8-32 UNC-2B X0.475
E_11-E_16	8-32 UNC-2B THRU
E_17-E_20	1/4-20 UNF-2B THRU
E_21-E_24	8-32 UNC-2B (HELICOIL) X0.243

UTA AERODYNAMICS REASEARCH CENTER		
PAGE: 1 OF E		
MATERIAL: ALUMINUM		
SCALE: 2:3	DRAWN BY: D.LEAMON	DATE: 16 AUG 2011
TOLERANCES:	.X	0.01
	.XX	0.001
	.XXX	0.001
	.XXXX	0.001

Front View

8.175
6.925
5.675
4.5
3.325
2.075
0.825

See Detail E3

E_3
E_4
E_2
E_5
E_18
E_17
E_1

E_7
E_6
E_19
E_8
E_9
E_20
E_10

E_12
E_21
E_13
E_15
E_23
E_11
E_22
E_14
E_16
E_24

2
1.1875
0.375

0.5
1.5

Front View

Top View

0.75
0.5
0.375
0.25

E_3
E_4
E_5
E_6
E_7
E_8

See Detail E2

Top View
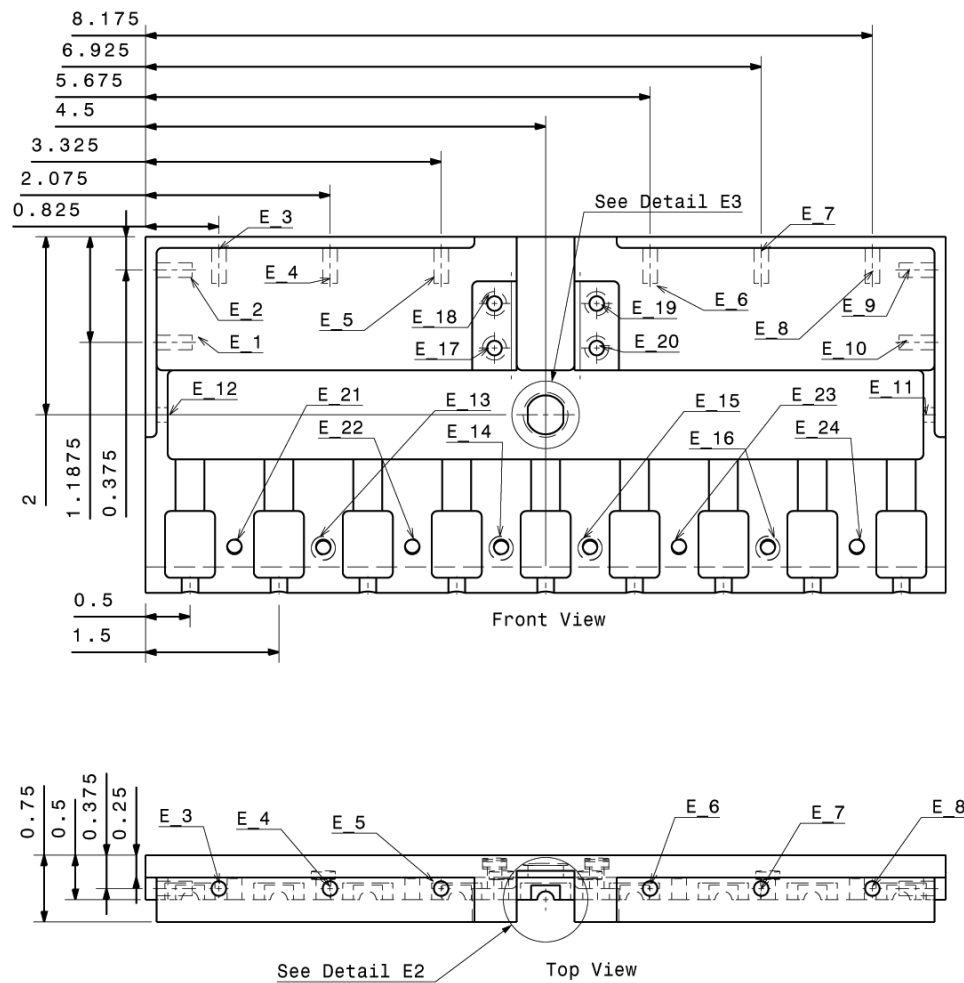
DIMENSIONS IN INCHES

Detail E3

∅0.502
0.4
∅0.4375

Detail E3
Scale: 2:1

Detail E2

0.65
0.575
0.5
0.25

Detail E2
Scale: 4:3

Fillets and Rounds: 1/16"

THREAD TABLE	
E_1-E_10	8-32 UNC-2B X0.475
E_11-E_16	8-32 UNC-2B THRU
E_17-E_20	1/4-20 UNF-2B THRU
E_21-E_24	8-32 UNC-2B (HELICOIL) X0.243

Auxiliary View
Scale: 1:1

0.085

E_13-E_16

Section View D-D
Scale: 1:1

E_13-E_16

∅0.27

0.5

93°

0.5151

E_21-E_24

87°

Section View C-C
Scale: 1:1

Front View

THREAD TABLE	
E_1-E_10	8-32 UNC-2B X0.475
E_11-E_16	8-32 UNC-2B THRU
E_17-E_20	1/4-20 UNF-2B THRU
E_21-E_24	8-32 UNC-2B (HELICOIL) X0.243

Fillets and Rounds: 1/16"

UTA AERODYNAMICS REASEARCH CENTER		
PAGE: 3 OF E		
MATERIAL: ALUMINUM		
SCALE: 2:3	DRAWN BY: D.LEAMON	DATE: 16 AUG 2011
TOLERANCES:	.X	0.01
	.XX	0.001
	.XXX	0.001
	.XXXX	0.001

Isometric View
Scale 1:3

DIMENSIONS IN INCHES

0.95

0.75

0.1

Section View A-A

Isometric View

$\emptyset$0.475

$\emptyset$0.35 $^{+0.002}_{0}$

0.2

$\emptyset$0.1875

A

A

Top View
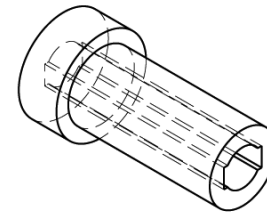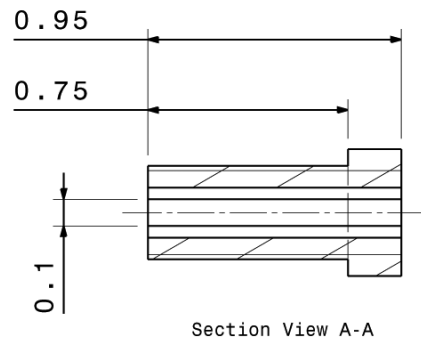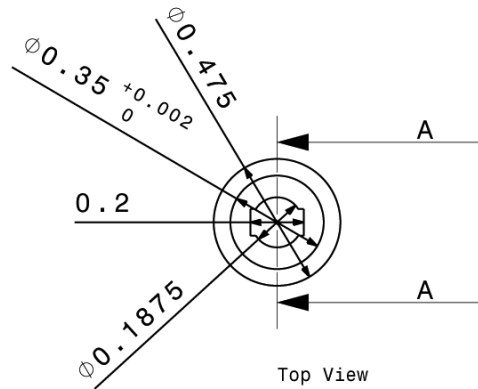
UTA AERODYNAMICS REASEARCH CENTER		
PAGE: 1 OF F		
MATERIAL: TEFLON		
SCALE: 2:1	DRAWN BY: D.LEAMON	DATE: 19 OCT 2011
TOLERANCES:	.XX	0.001
	.XXX	0.001
	.XXXX	0.001

DIMENSIONS IN INCHES

$\phi 0.75$

$\phi 0.49$

$\phi 0.35$

$\phi 0.2$

G_1

Bottom View

Isometric View

R0.375

A

1.325

0.575

G_1

0.375

Section View A-A

1.2

A

Front View
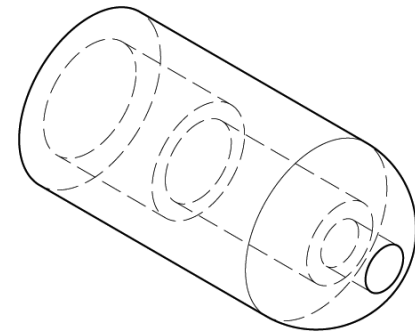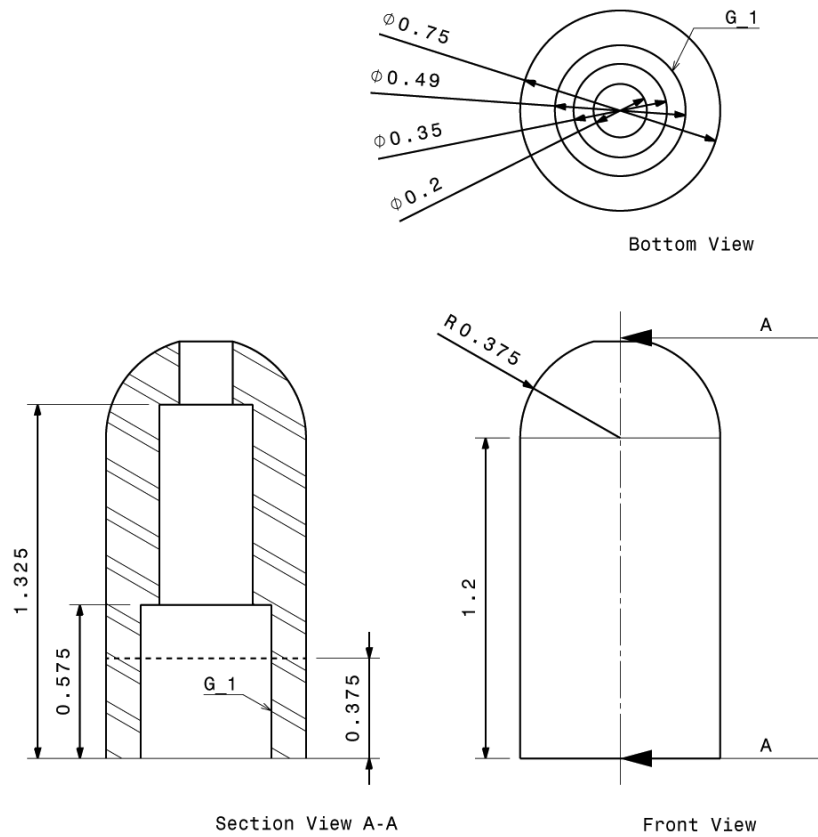
DIMENSIONS IN INCHES

THREAD TABLE	
G_1	1/2-20 UNF-2B X0.375

UTA AERODYNAMICS REASEARCH CENTER			
PAGE: 1 OF G			
MATERIAL: ALUMINUM			
SCALE: 2:1	DRAWN BY: D.LEAMON	DATE: 21 JUNE 2011	
TOLERANCES:		.X	0.01
		.XX	0.001
		.XXX	0.0005
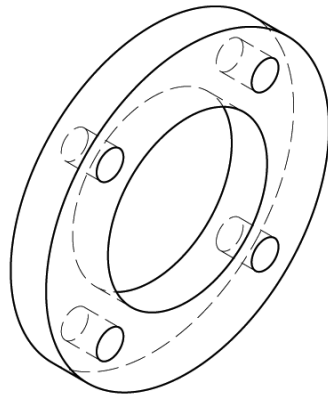
Isometric View

Section View A-A

0.775

0.25

45°

∅0.19

A

∅1.125

∅2

Top View
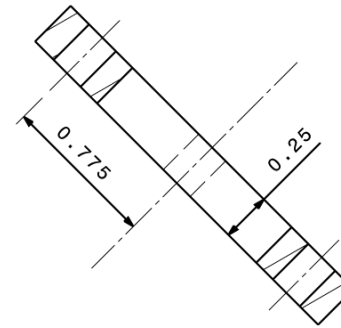
A
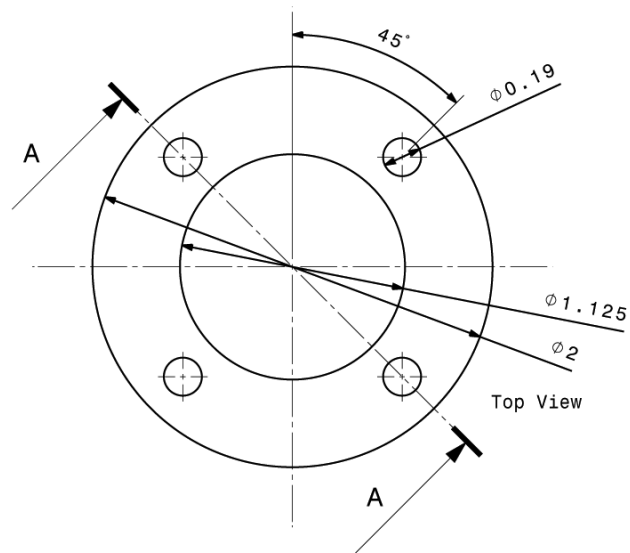
DIMENSIONS IN INCHES

UTA AERODYNAMICS REASEARCH CENTER		
PAGE: 1 OF H		
MATERIAL: ALUMINUM		
SCALE: 3:2	DRAWN BY: D.LEAMON	DATE: 24 AUG 2011
TOLERANCES:	.X	0.01
	.XX	0.001
	.XXX	0.001

R0.325

I_1 I_2

4.175

1.75

1.5

Right View

Fillets and Rounds: 1/16"

Φ0.4

Top View

0.65

0.45

0.2

I_1

Φ0.164

Front View

0.75

0.25

1

1.65

1.15

0.5

0.25

1.4

Bottom View
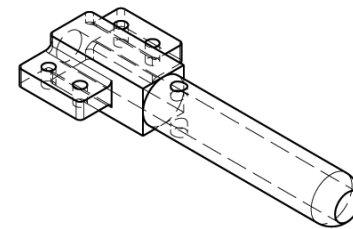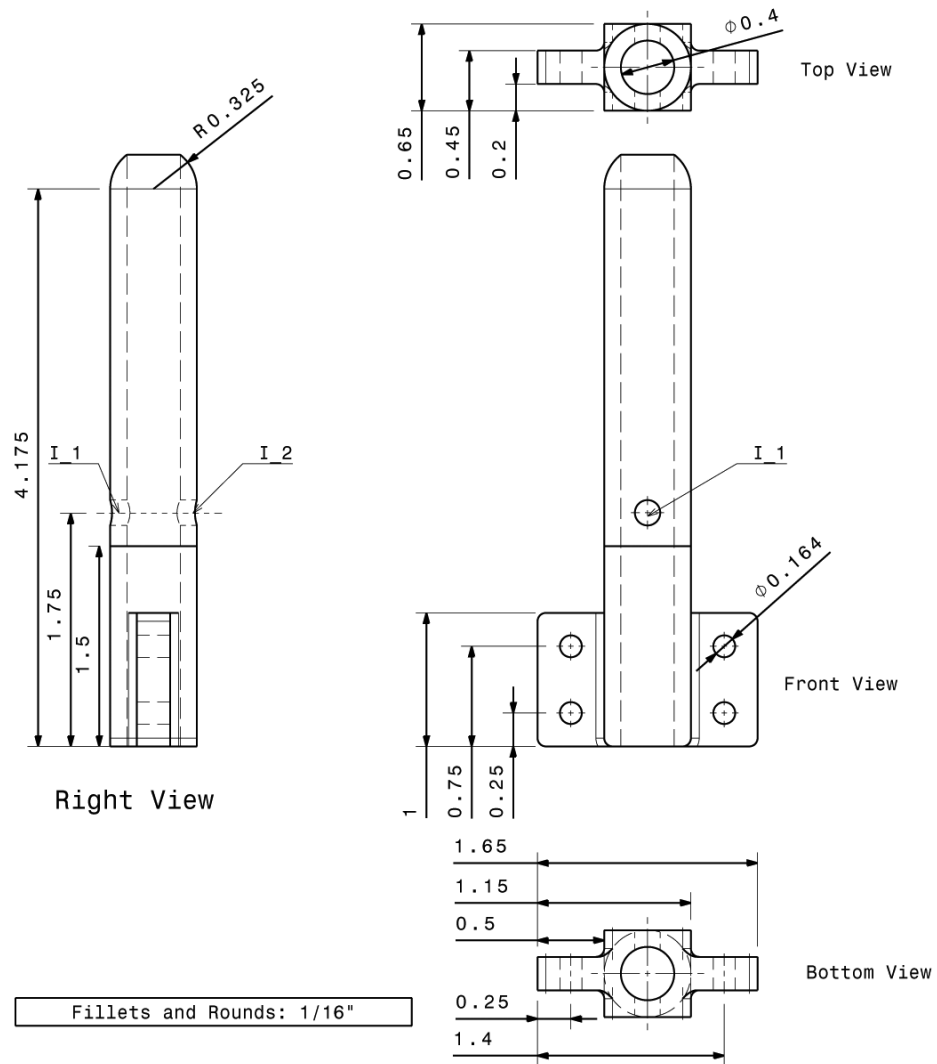
Isometric View
Scale: 2:3

DIMENSIONS IN INCHES

THREAD TABLE	
I_1-I_2	10-32 UNC-2B THRU

UTA AERODYNAMICS REASEARCH CENTER		
PAGE: 1 OF I		
MATERIAL: ALUMINUM		
SCALE: 1:1	DRAWN BY: D.LEAMON	DATE: 16 AUG 2011
TOLERANCES:	.X	0.01
	.XX	0.001
	.XXX	0.001

84

Bottom View

1.143
0.893
0.275

J_1

J_2

0.375
0.814
1.064

Isometric View

∅0.25

J_1

∅0.5

J_1

0.398

Detail J1
Scale: 3:1

0.375

See Detail J1

J_2

Front View
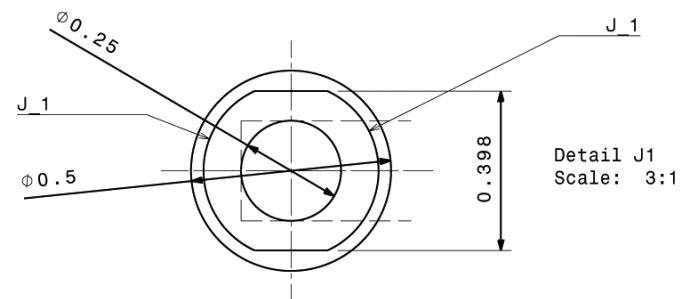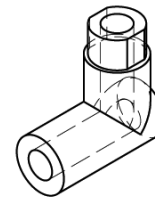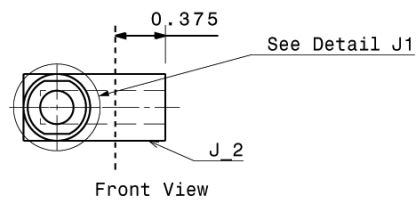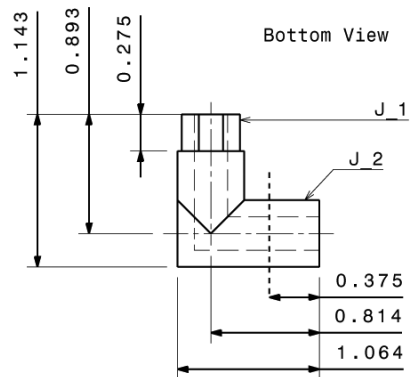
THREAD TABLE	
J_1	7/16-28 UNEF-2B X0.275
J_2	1/2-20 UNF-2A X0.400

UTA AERODYNAMICS REASEARCH CENTER			
PAGE: 1 OF J			
MATERIAL: ALUMINUM			
SCALE: 2:1	DRAWN BY: D.LEAMON	DATE: 15 AUG 2011	
TOLERANCES:		.X	0.01
		.XX	0.001
		.XXX	0.001

DIMENSIONS IN INCHES

Bottom View

Isometric View

0.748

0.515

0.475

0.395

0.5615

0.373

0.1855

0.2803

Right View

See Detail K1

Left View

Front View   K_1

Quantity Needed: 9

Ø0.277

Ø0.25 $^{+0.003}_{0}$

Ø0.221 ±0.002

Detail K1
Scale: 5:1

K_1

Fillets and Rounds: 1/16"

DIMENSIONS IN INCHES

THREAD TABLE	
K_1	5/16-24 UNF-2B X0.400

UTA AERODYNAMICS REASEARCH CENTER			
PAGE: 1 OF K			
MATERIAL: ALUMINUM			
SCALE: 2:1	DRAWN BY: D.LEAMON	DATE: 15 AUG 2011	
TOLERANCES:		.X	0.01
		.XX	0.001
		.XXX	0.001
		.XXXX	0.001
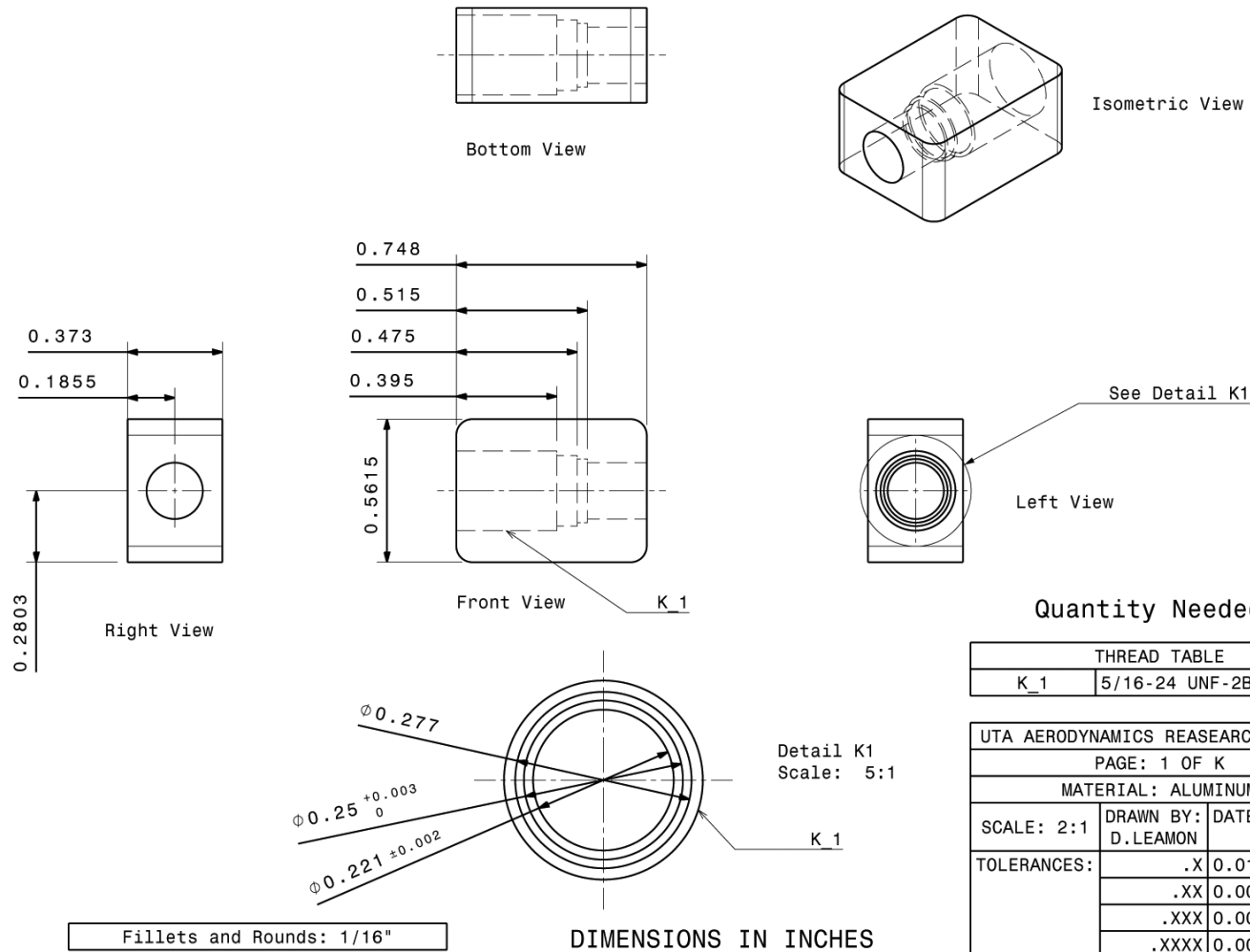
APPENDIX B

MATLAB® CODES [15]

Sample Low-Pass Butterworth Filter Code Used on Transducer and RTD Output

```matlab
clc;clear;
fi1 = fopen('Data1.csv');              % input data file
f1 = textscan(fi1, '%f %f %f %f %f %f %f %f %f %f', 'Delimiter',
',','HeaderLines',23);
fclose(fi1);
time =f1{1};
PCB1 =f1{2};
PCB2 =f1{3};
PCB3 =f1{4};
PCB4 =f1{5};
PCB5 =f1{6};
PCB6 =f1{7};
PCB7 =f1{8};
PCB8 =f1{9};
PCB9 =f1{10};

Fs=2500000;                            % frequency
Fc=20000;                              % filter cutoff frequency
cutof_freq= Fc/(Fs/2);
[B,A] = butter(1,cutof_freq);

pp1=filter(B,A,PCB1);                  % filtered vs unfiltered plots
pp1=pp1-mean(pp1(1:1000));
plot(time,PCB1)
hold on
plot(time,pp1,'r')

X = [time,pp1,pp2,pp3,pp4,pp5,pp6,pp7,pp8,pp9];
X = transpose(X);
fileID = fopen('Data1.txt','w');       % output text file
fprintf(fileID,'%10s %13s %13s %13s %13s %13s %13s %13s %13s
%13s\r\n','TIME','PCB1','PCB2','PCB3','PCB4','PCB5','PCB6','PCB7','PCB
8','PCB9');
fprintf(fileID,'%+9.7f %+10.10f %+10.10f %+10.10f %+10.10f %+10.10f
%+10.10f %+10.10f %+10.10f %+10.10f\r\n',X);
fclose(fileID);
```

Sample Cook-Felderman and Temperature Plot Codes Used on RTD Output

```
clc;clear;
%% Cook-Felderman

%RTD#2 Data
tp = 0.20255327;          % Thermal Product
a = 0.001212963;          % Temperature Resistance Coefficient

fi1 = fopen('RTD2x.csv');   % Input Data File
f1 = textscan(fi1, '%f %f %f', 'Delimiter', ',','HeaderLines',1);
fclose(fi1);
t = f1{1};                % Time
V2 = f1{2};               % Voltage
V = f1{3};                % Poly-Fit

f = 2500000;              % Frequency
d = 1/f;                  % Delta t

plot(t,V,t,V2,'r','linewidth',2)
axis([0 0.001 0 0.025]);

V0 = 4;
n = length(V);

for i=2:n-1;                % Cook-Felderman
    x(i) = ((V(n)-V(i))/(sqrt(t(n)-t(i))))-((V(n)-V(i-1))/(sqrt(t(n)-
t(i-1))))+2*((V(i)-V(i-1))/((sqrt(t(n)-t(i)))+(sqrt(t(n)-t(i-1)))));
    qdot = (tp/((sqrt(pi()))*a*V0))*((V(n)/(sqrt(t(n))))+x+((V(n)-V(n-
1))/(sqrt(d))));
end

qdot(1) = qdot(2);
qdot(n) = qdot(n-1);

AVG = mean(qdot(10:1000))    % Calculated Heat Flux

figure
plot(t,qdot,'k');
axis([0 0.0005 0 100]);
xlabel('Time (s)');
ylabel('Heat Flux (W/cm^2)');
title('Heat Flux Correlation');
legend('Cook-Felderman Algorithm');

%% Temperature Plot
fi2 = fopen('RTD2.csv');    % Input Data File
f2 = textscan(fi2, '%f %f', 'Delimiter', ',','HeaderLines',14);
fclose(fi2);
t2 = f2{1};               % Time
e  = f2{2};               % Voltage
```

```matlab
b  = 35.179/0.0524;          % Deg C/Volts

Fc=20000;                    % Cutoff Frequency
cut= Fc/(f/2);
[B,A] = butter(1,cut);       % Butterworth Filter

e  = (e-mean(e(1:100)))*b+25;
e2  = filter(B,A,e);

figure
plot(t2,e,t2,e2,'r');
axis([-.0005 0.002 0 70]);

%% Square-Root of Time Linear Regression
fi2 = fopen('RTD2y.csv');    % Input Data File
f2 = textscan(fi2, '%f %f %f %f %f', 'Delimiter',
',','HeaderLines',14);
fclose(fi2);
t3 = f2{1};
rtd = f2{2};
lin = f2{3};                 % linear fit data
con1 = f2{4};                % confidence line data
con2 = f2{5};                % confidence line data

figure
plot(t3,rtd,'k',t3,lin,'-',t3,con1,'-r',t3,con2,'-g');
```

REFERENCES

1. Stuessy, W. Scott, "Hypersonic Shock Tunnel Development and Calibration," Master's Thesis, Department of Aerospace Engineering, The University of Texas at Arlington, Arlington, TX, 1989.

2. Kinnear, Kevin M., "Design, Calibration and Testing of Transient Thin Film Heat Transfer Gauges," Master's Thesis, Department of Mechanical and Aerospace Engineering, The University of Texas at Arlington, Arlington, TX, 1997.

3. Anderson, John D., Jr.: *Modern Compressible Flow: With Historical Perspective,* 3d ed., Mcgraw-Hill Book Company, New York, 2003.

4. Chung, Kung-Ming, "Shock Impingement Near Mild Hypersonic Expansion Corners," Ph.D Dissertation, Department of Aerospace Engineering, The University of Texas at Arlington, Arlington, TX, 1992.

5. Cone Chart. BigCeramicStore.com. 29 Apr. 2012
<http://www.bigceramicstore.com/information/ConeChart.html>

6. Eckert, E. R. G., and R. M. Drake., *Analysis of Heat and Mass Transfer*, McGraw-Hill, New York, 1972.

7. CEARUN. Ed. Dr. Michael J. Zehe. NASA. 22 Mar. 2012 <http://cearun.grc.nasa.gov/>

8. Anderson, John D., Jr., *Fundamentals of Aerodynamics*, 4th ed., McGraw-Hill, New York, 2007.

9. Reynolds Number. Ed. Tom Benson. 22 May 2009. NASA. 22 Mar. 2012
<http://www.grc.nasa.gov/WWW/BGH/reynolds>

10. Saravanan S., Jagadeesh G., and Reddy K. P. J., "Aerodynamic Force Measurement Using 3-Component Accelerometer Force Balance System in a Hypersonic Shock Tunnel," Springer-Verlag, 2008

11. Mee, David J., "Dynamic Calibration of Force Balances," Department of Mechanical Engineering, The University of Queensland, Australia, Report Number 2002/6, 2003.

12. Figliola, R.S. and Beasley, D.E., *Theory and Design for Mechanical Measurements*, 5th Edition, John Wiley & Sons, Inc., 2011, pp. 164-168.

13. Cook W. J. and Felderman E. J., "Reduction of Data from Thin-Film Heat-Transfer Gages: A Concise Numerical Technique," AIAA Journal, Vol. 4, No, 3, 1966, pp.561.

14. Lassaline, J.V., "Supersonic Right Circular Cone at Zero Angle of Attack," Department of Aerospace Engineering, Ryerson University, Toronto, Ontario, Canada 2009.

15. MATLAB (2008b, The MathWorks, Natick, Massachusetts, U.S.A.)

BIOGRAPHICAL INFORMATION

Derek Leamon was born in Dallas, Texas on September 26th, 1984. After developing an interest in aircraft and spacecraft in high school, he pursued and received a Bachelor of Science in Aerospace Engineering from The University of Texas at Arlington in 2008. After a difficult and unrewarding job hunt, Derek returned to UT Arlington a year later seeking higher education by pursuing a Masters degree from the same department he had left. During his first year in the Masters program, Derek took multiple Air Breathing Propulsion courses through Dr. Wilson that led to the opportunity of pursuing an experimentally based thesis in the Aerodynamics Research Center.